

A Comparison of Two Vertical Mixing Schemes in a Pacific Ocean General Circulation Model

Xianjin Li^{1*}, Yi Chao^{1*}, James C. McWilliams²
and
Lee-Lueng Fu¹

January 18, 2000

1. Jet Propulsion Laboratory, California Institute of Technology

2. University of California at Los Angeles

Submitted to *Journal of Climate* on 3 May 1999; Revised on January 2000

*Corresponding address:

M/S 300-323, JPL

4800 Oak Grove Drive

Pasadena, CA 91109-8099

Phone: 818-354-6654 or 818-354-8168

E-mail: xjl@pacific.jpl.nasa.gov or yc@pacific.jpl.nasa.gov

Abstract

The upper Pacific Ocean current and temperature have been simulated by a 3-dimensional ocean general circulation model (OGCM) with two different vertical mixing schemes. One corresponds to the modified Richardson number dependent scheme of Pacanowski and Philander (PP, 1981); the other is adapted from the newly developed K-Profile Parameterization (KPP) scheme (Large et al., 1994). Both schemes include the penetration of shortwave radiation. For the KPP scheme, an ocean boundary layer depth is predicted and the turbulent mixing within this boundary layer is parameterized using a nonlocal bulk Richardson number and the similarity theory of turbulence. Below the boundary layer, the vertical mixing is parameterized through the local gradient Richardson number and a background mixing coefficient similar to the PP scheme. The performances of both schemes in the Pacific OGCM are evaluated under the same model configuration and boundary conditions. Model and data comparisons are made for the mean state, annual cycle, and interannual-to-interdecadal variability. In the tropics, both the PP and KPP schemes produce reasonably realistic tropical thermal and current structures; however, the KPP is better than the PP in several important aspects. For example, the thermocline in the KPP scheme is tighter and the cold tongue in the eastern equatorial Pacific is less cold than that in the PP solution. The core of the equatorial Undercurrent from the KPP scheme is much closer to the observation. In the extra-tropics, however, the KPP scheme is significantly better than the PP in simulating the thermal and current structures ranging from the mean state to annual cycle and decadal-to-interdecadal variability.

1. Introduction

It is well-known that oceanic vertical mixing plays a prominent role in regulating the sea surface temperature (SST), a critical oceanic parameter in controlling the exchanges of energy and momentum between the ocean and atmosphere. Climate models with an aim to represent realistic ocean dynamics have to properly describe the vertical mixing processes. The vertical mixing, because of the small-scale turbulent processes involved, usually cannot be explicitly resolved in ocean general circulation models (OGCMs) and has to be parameterized.

The conventional parameterization of the vertical mixing is to use an eddy diffusion model (the so-called K-theory), which assumes a local relationship between eddy fluxes and model prognostic variables. The simplest example is to use a constant mixing coefficient everywhere (Bryan and Lewis, 1979; Sarmiento and Bryan, 1982). Although the constant mixing coefficient can be optimized for some specific regions, its application to models of basin to global scales is often problematic. One alternative is to relate the mixing coefficients to the local Richardson number (Ri) based on stability theory (Robinson, 1966). The Ri -dependent mixing scheme was demonstrated to have a reasonable skill in simulating the tropical circulation in 3-dimensional OGCMs (Pacanowski and Philander, 1981, hereafter as PP; Philander et al., 1987). Simulations with the PP scheme provide a good representation of the shear instability process in the tropical oceans. Therefore, they are significantly better in the tropics than those with constant mixing coefficients. However, the PP scheme is still deficient in simulating several important aspects of the tropical circulation (Stockdale et al., 1993; Niiler et al., 1995). Comparison with turbulence measurements has shown that the PP scheme underestimates the turbulent mixing at low Ri , while overestimating the turbulence mixing at high Ri (Peters et al., 1988). As a result, the thermocline simulated by the PP scheme is much too diffused as compared to observations. The surface current simulated

by the PP scheme is too strong, while the Equatorial Undercurrent is too shallow due to insufficient momentum penetration in the surface boundary layer (Niiler et al., 1995; Halpern et al., 1995). Furthermore, the performance of the PP scheme in the extra-tropics is rather poor (Stammer et al., 1996) due to the lack of explicit specification of other turbulence mixing processes (e.g., wind stirring and convective overturning). The PP scheme is essentially a first-order turbulence closure scheme involving a parameterization of small-scale Kelvin-Helmholtz instability. It is not meant to parameterize the effects of large eddies. All these motivate further exploration of alternative vertical mixing schemes (e.g., Waliser et al., 1994).

One alternative is to use higher-order turbulence closure schemes: e.g., the second-order closure scheme of level-1.5 (Blanke and Delecluse, 1993), level-2.5 (Mellor and Yamada, 1982; Rosati and Miyakoda, 1988), or a modified second-order closure mixed-layer scheme (Kantha and Clayson, 1994). However, most of these higher-order closure schemes require high vertical resolution and/or high-frequency forcings and are, therefore, computationally costly for climate studies. These turbulence closure schemes attempt to parameterize small-scale motions with local prognostic variables in the model such as turbulence length scales, which are small in comparison to the boundary layer. Gnanadesikan and Weller (1995) and McWilliams et al. (1997) have argued that such schemes are unstable to large eddies, such as those in the Langmuir circulation. Meanwhile, the lack of explicit nonlocal turbulence transport in these turbulence closure schemes strongly limits their representation of the subgrid-scale mixing processes due to the difficulty in reproducing the entrainment flux at the bottom of the boundary layer (Ayotte et al., 1996).

Another alternative is to employ a vertically homogeneous mixed-layer model (e.g., Kraus and Turner, 1967; Garwood, 1977) to simulate the near surface processes. Using a layered model, Chen et al. (1994) recently developed a hybrid scheme by combining a homogeneous

mixed-layer model with Price's (Price et al., 1986) dynamical instability model. However, the coupling of such a bulk mixed-layer model to a discrete level model is far from straightforward (Haidvogel and Beckmann, 1999).

Recently a nonlocal vertical mixing scheme called K-Profile Parameterization (KPP) has been proposed (Large et al., 1994). The KPP scheme does not assume *a priori* that the boundary layer is well mixed and explicitly predicts an ocean boundary layer depth. Within this boundary layer, the turbulent mixing is parameterized using a nonlocal bulk Richardson number and the similarity theory of turbulence. Below the boundary layer, the vertical mixing is parameterized through the local gradient Richardson number and a background mixing similar to the PP scheme.

The KPP formulation and its performance in one-dimensional models have been described in Large et al. (1994) and Large and Gent (1999). The annual-mean climatology from a 3-dimensional coarse-resolution global ocean model with the KPP scheme can be found in Large et al. (1997), where numerical experiments are designed for comparison with a baseline experiment with constant vertical mixing coefficients. What is the performance of the KPP scheme in a higher resolution ocean general circulation model? Besides the annual-mean climatology, what kind of systematic impact does the KPP scheme have on simulating the important annual cycle and interannual-to-interdecadal variability? How significant are those improvements of the KPP scheme, if any, in simulating the thermal and current structures when compared with those conventional schemes? This paper describes the performance of the KPP scheme in simulating the 3-dimensional thermal and current structures in a Pacific OGCM with enhanced resolutions in the tropics. Systematic comparisons are made between the KPP and PP schemes in terms of the annual-mean climatology, annual cycle, and interannual-to-interdecadal variability. The description of the ocean model and model

experiments is given in section 2. In section 3, both mixing schemes are described briefly. In section 4, the comparisons between the simulations and available observations are made. Finally, discussion and summary are presented in section 5.

2. Description of ocean model and experiment design

2.1 The model

The numerical model used in this study is based upon the National Center for Atmospheric Research (NCAR) Climate System Modeling (CSM) Ocean Model (NCOM) (Gent et al., 1998), which evolved from the Modular Ocean Model (Pacanowski, et al. 1991) developed at the Geophysical Fluid Dynamical Laboratory (GFDL). Among several new features implemented in NCOM, we want to emphasize the eddy-induced isopycnal transport parameterization (Gent and McWilliams, 1990, hereafter as GM) and the KPP vertical mixing scheme, which will be explained in details in section 3. The governing equations are the primitive equations in spherical coordinates, with the hydrostatic, Boussinesq, and rigid-lid approximations (Bryan, 1969; Cox, 1984). The model domain covers the Pacific basin from 45°S to 65°N in latitude and from 100°E and 70°W in longitude. The longitudinal resolution is 2° uniformly. The latitudinal resolution is 0.5° within 10°S and 10°N and gradually increases poleward to 2° at and beyond 20°S and 20°N. There are 25 levels throughout the water column, with 5 uniform levels in the upper 50 m and 10 additional levels between 50 and 277 m (see Table 1). Because of the use of the GM parameterization, the horizontal diffusivity is set to zero and a relatively small value of $5 \times 10^5 \text{ cm}^2 \text{ s}^{-1}$ is used for horizontal viscosity, isopycnal diffusivity, and thickness diffusivity. The vertical mixing terms are treated implicitly. The time step is one hour.

The parameterization schemes for the surface fluxes and the vertical mixing are described

in more details below, since they are intimately coupled with the ocean boundary layer parameterization.

2.2 Surface forcing

Surface forcing can be separated into momentum, heat, and fresh-water fluxes. The momentum fluxes (τ_u, τ_v) are calculated from the zonal and meridional wind speeds in the Comprehensive Ocean-Atmospheric Data Set (COADS) (da Silva et al., 1994) by using the formula based on the Large and Pond (1981) drag formulation. The COADS is selected because it is the longest surface marine data set covering the whole Pacific basin. The net heat flux Q_t across the ocean surface is given as:

$$Q_t = R_S - R_L - Q_S - Q_L, \quad (1)$$

where R_S is the incoming short wave radiation and R_L is the outgoing long wave radiation. Both R_S and R_L are provided by COADS. The sensible heat flux Q_S and the latent heat flux Q_L are calculated through the bulk formula as follows:

$$Q_S = \rho_o C_D C_P |V| (T - T_A) \quad (2)$$

$$Q_L = \rho_o C_D L |V| [e_s(T) - \gamma e_s(T_A)] (0.622/P_A), \quad (3)$$

where $|V|$ is the wind speed, T_A is the air temperature (both also derived from COADS), and T is the model simulated temperature. The saturation vapor pressure is

$$e_s(T) = 10^{9.4 - \frac{2353}{T}}. \quad (4)$$

The constants are $\rho_o = 1.2 \times 10^{-3} \text{ g cm}^{-3}$, $L = 595 \text{ cal g}^{-1}$, $C_D = 1.2 \times 10^{-3}$, $C_P = 0.24 \text{ cal g}^{-1} \text{ } ^\circ\text{C}^{-1}$, $P_A = 1013 \text{ mb}$, and the mixing ratio $\gamma = 0.8$. The parameterizations of the kinematic surface

fluxes are given by

$$\overline{wu_0} = -\frac{\tau_u}{\rho_0} \quad (5)$$

$$\overline{wv_0} = -\frac{\tau_v}{\rho_0} \quad (6)$$

$$\overline{wt_0} = -\frac{Q_t}{\rho_0 C_{p0}}. \quad (7)$$

For the model salinity, the climatological fresh-water flux, F_t , defined as the precipitation minus evaporation, derived from COADS, is used. In order to compensate uncertainties in the fresh-water flux, the model sea surface salinity is also restored toward the value of Levitus monthly-mean climatology (Levitus et al, 1994) with a damping time scale of thirty days. The parameterized fresh-water flux is:

$$\overline{ws_0} = F_t \frac{S_0}{\rho_0} + \gamma_s (S_{Levitus} - S), \quad (8)$$

where $\gamma_s = dz(1)/30days$, where $dz(1)$ is the first-level grid depth. The surface buoyancy flux $\overline{wb_0}$ and buoyancy forcing B_f and the buoyancy profile $B(z)$ are calculated as

$$\overline{wb_0} = g(\alpha \overline{wt_0} - \beta \overline{ws_0}) \quad (9)$$

$$B_f = -\overline{wb_0} \quad (10)$$

$$B(z) = g(\alpha T - \beta S), \quad (11)$$

where g is gravitational acceleration, α and β are the thermodynamic expansion coefficients evaluated at local values of T and S , and the subscript 0 specifies the value at the surface.

2.3 Experiment Design

The annual mean climatological temperature and salinity distributions of Levitus et al. (1994) are used for model initial conditions. The model ocean was spun up for 30 years

from rest using the COADS monthly-mean climatological wind stress, heat, and fresh water fluxes (da Silva et al., 1994). The short-wave radiation is allowed to penetrate below the model ocean surface, leading to sub-surface bulk heating using the formula of Paulson and Simpson (1977). For this spin-up experiment, as in Barnier et al. (1995), the model heat flux has two components: a prescribed COADS net flux and a correction term proportional to the difference between the COADS climatological SST and the model SST. The correction coefficient is computed based on air-sea variables and is a function of space and time. The COADS monthly-mean climatological evaporation and precipitation rates are used to calculate the model fresh-water flux. In order to compensate errors in the fresh-water flux, the surface salinity is restored toward the Levitus monthly-mean climatology with a restoring time scale of 30 days. After 30 years of model integration, the upper ocean reaches a quasi-equilibrium state. Then, the real-time monthly-mean COADS wind stress from January 1945 to December 1993 is used to force the model ocean. The heat flux is calculated as described in the previous section. Two 49-year (1945-1993) solutions have been obtained. The two simulations differ from each other only by the vertical mixing schemes: i.e., PP versus KPP, which is explained in the following section.

3. The vertical mixing schemes

3.1 The Pacanowski and Philander (PP) scheme

With the PP scheme, turbulent mixing in an ocean general circulation model is treated by a first-order local diffusion approach in which the subgrid-scale turbulent vertical kinematic flux of a quantity x (X as the mean) is assumed proportional to the local property gradient with an appropriate eddy mixing coefficient K . This so-called K -theory can be described as

$$\overline{wx} = -K\partial_z X, \quad (12)$$

where the upper case (X) represents mean quantities resolved at the model grid and the lower case (x) represents the subgrid scale variables (also called turbulent fluctuations). The measurements of Crawford and Osborn (1979) and Osborn and Bilodean (1980) suggest that turbulent mixing processes in the tropics are strongly influenced by the shear of the mean currents. The mixing coefficients can be approximated as

$$K_m = \frac{\nu_0}{(1 + \alpha Ri_g)^n} + \nu_b \quad (13)$$

$$K_t = \frac{\nu_0}{(1 + \alpha Ri_g)^{n+1}} + \kappa_b, \quad (14)$$

where K_m represents viscosity, K_t represents diffusivity, and the local gradient Richardson number

$$Ri_g = \frac{N^2}{U_z^2 + V_z^2}. \quad (15)$$

As in Pacanowski and Philander (1981), the background viscosity $\nu_b = 1.0 \text{ cm}^2 \text{ s}^{-1}$, diffusivity $\kappa_b = 0.1 \text{ cm}^2 \text{ s}^{-1}$, $\nu_0 = 100 \text{ cm}^2 \text{ s}^{-1}$, $n = 2$, and $\alpha = 5$. N represents Vaisala frequency and U_z and V_z the vertical shear. In particular, at the model's first level, both K_m and K_t have a minimum value of $10 \text{ cm}^2 \text{ s}^{-1}$ to compensate for the mixing induced by the high-frequency wind fluctuations that are absent from the monthly mean values. For the convection case ($Ri_g < 0$), a maximum value of $1.0 \times 10^6 \text{ cm}^2 \text{ s}^{-1}$ is used in order to mix the heat instantaneously in the vertical to a depth that ensures a stable density gradient.

3.2 The K-Profile Parameterization (KPP) scheme

In contrast to the conventional PP scheme, the KPP scheme considers two distinctly nonlocal aspects of large-scale ocean turbulence. The subgrid-scale, turbulent, vertical kinematic flux can be described as

$$\overline{w\bar{x}} = -K(\partial_z X - \gamma_x), \quad (16)$$

where the term γ_x represents the additional nonlocal transport term besides the familiar local downgradient component. The eddy mixing coefficient K everywhere inside the ocean boundary layer (OBL) depends upon both the surface forcing and the depth of the layer as follows:

$$K(\sigma) = hw(\sigma)G(\sigma), \quad (17)$$

where $\sigma = \frac{d}{h}$ represents a dimensionless vertical coordinate, h the OBL depth, d the distance from the surface, $w(\sigma)$ a depth-dependent characteristic velocity called turbulent velocity scale, and $G(\sigma)$ a nondimensional vertical shape function. Equation (16) is applied for temperature, salinity, and other passive tracers. The eddy viscosity, K_m , is also defined as (16) but with w replaced by another velocity scale w_m . With proper formulation of w (or w_m), it can be shown that Equation (16) behaves well from very stable to very unstable conditions in horizontally homogeneous and quasi-stationary situations (Högström, 1988; Large et al., 1994). For unstable conditions, w and w_m are proportional to the so-called convective velocity scale w_* , while for neutral and stable conditions, w and w_m are proportional to the friction velocity u_* . A summary of the velocity scales is given in Appendix A.

The depth of the OBL is determined by a bulk Richardson number relative to the surface as:

$$Ri_b = \frac{(B_r - B)d}{(U_r - U)^2 + (V_r - V)^2 + V_t^2}, \quad (18)$$

when $Ri_b = Ri_c$ (a critical value of 0.3 used in our simulation), the depth is called boundary layer depth h . It measures how deep a turbulent boundary layer eddies with a mean velocity (U_r, V_r) and mean buoyancy B_r can penetrate into the interior stratification before becoming stable relative to the local buoyancy and velocity. Both B_r and (U_r, V_r) are estimates of the average buoyancy and velocity, respectively, over the surface thin layer on the top of h . In our simulation, since our vertical resolution is rather coarse, they are simply set to the values

at the surface first level. The turbulent velocity shear term V_t/d measures the strength of the turbulence and is important in pure convection and other situations of little or no mean shear. Its detailed definition can be found in Appendix B. Because of the addition of V_t , h can measure the strength of the entrainment from the stratified layer below the surface mixed-layer due to the large turbulent eddies.

At all depths inside the OBL, the mixing coefficients are directly proportional to h , reflecting the ability of deeper boundary layers to contain larger, more efficient turbulent eddies. The shape function is a cubic polynomial (O'Brien, 1970) as:

$$G(\sigma) = \sigma(1 + a_2\sigma + a_3\sigma^2). \quad (19)$$

Obviously, $G(0) = 0$ satisfies the physical condition that turbulent eddies do not cross the surface. The coefficients a_2 and a_3 are computed to make the interior and boundary layer mixing coefficients and their gradients match at $\sigma = 1.0 (d = h)$. Thus, interior mixing is able to influence the entire boundary layer.

The nonlocal transport term γ_x in Equation (15) represents the nonlocal impact of the large-scale turbulence mixing and is non-zero only in the boundary layer for tracers under unstable forcing for our present simulations. The detailed description of γ_x can be found in the Appendix C. Below the boundary layer h , the parameterization is similar to the PP case where both viscosity and diffusivity are shear-dependent.

4. Results

In order to distinguish the difference between the KPP and PP simulations, a detailed comparison is made in this section by separating the simulated 49-year time-series into the annual mean state, annual cycle, and interannual-to-interdecadal variability. All the

mean states are calculated within the period from 1961 to 1990 unless specifically mentioned otherwise.

4.1 The Mean State

a. Tropics

The coefficients of vertical eddy viscosity K_m and eddy diffusivity K_t vary considerably in the global oceans. They usually have large values in the surface mixed-layer, but have very small values below the thermocline. Figure 1 shows the vertical profile of mean K_m on the equator at 165°E, 140°W, and 110°W, respectively. As a remarkable difference in the surface of 50-100 m, K_m from the KPP scheme is much larger than K_m from the PP scheme. For the KPP scheme, as observed by Crawford and Osborn (1979), K_m varies from $10\text{cm}^2\text{s}^{-1}$ to $100\text{cm}^2\text{s}^{-1}$ in the top 50 m water column in both the central and eastern equatorial Pacific Ocean. In the western warm pool region, K_m can be even larger, with a value of $250\text{cm}^2\text{s}^{-1}$ at the surface. As expected, the simulated value of K_m in and below the thermocline, however, is substantially smaller. Figure 2 shows the vertical distribution of simulated mean zonal velocity on the equator for comparison with the mean Tropical Atmosphere Ocean (TAO) array observation (Yu and McPhaden, 1999) at 165°E, 140°W, and 110°W, respectively. Note that the Equatorial Undercurrent (EUC) at 140°W in the KPP solution is much deeper and the depth of its core is about 20 meters closer to the observation than that in the PP solution. This can be explained as follows: a larger vertical eddy viscosity is parameterized in the KPP scheme and, therefore, more surface kinetic energy can penetrate into the deeper ocean interior across the sharp thermocline through the resolved surface boundary layer. The improvement in the western equatorial Pacific is also remarkable, even though the contribution from the Indonesia throughflow can not be ignored in reality. At

the location of 110°W , even the amplitude of EUC is much weaker in both solutions than TAO observation there. This is probably caused by insufficient vertical resolution in the thermocline out-cropped region. The depth of EUC core in the KPP solution is also much closer to the observed than in the PP solution.

Besides the improvement in simulating the mean tropical current structure, the KPP scheme also produces more realistic thermal structure than the PP scheme. Figure 3 shows the annual-mean temperature along the equator and the differences between the two simulations and the Levitus climatology (Levitus et al., 1994). The thermocline in the KPP solution is more tightly defined than the PP solution due to the larger value of K_t , although both solutions are colder than the Levitus annual-mean climatology (mostly due to errors in the surface heat flux). Figure 4 shows the annual-mean SST and the differences between the simulations from both the KPP and PP schemes and the Levitus climatology. When the PP scheme is used, the simulated temperature in the eastern equatorial Pacific Ocean can be more than two degrees colder than the observed (Fig. 4e). This cold bias as described in Stockdale et al. (1993) and Niiler et al. (1995) in the eastern equatorial Pacific is significantly reduced to less than one degree when the KPP scheme is used (Figure 4d).

b. Extratropics

In the extratropical region, where shear-dependent mixing is significantly weaker than in the tropical region, the difference can be even more dramatic. This is clearly shown in Figure 5, where the mean K_m averaged over the central North Pacific region (160°E - 160°W , 34° - 36°N) is displayed. For the KPP scheme, K_m varies from $10\text{cm}^2\text{s}^{-1}$ to $40\text{cm}^2\text{s}^{-1}$ inside the surface mixed layer. On the other hand, the PP scheme obviously failed to simulate the vertical eddy viscosity. Similarly, the simulated current structure is different. The mean zonal current and its Ekman component in the central North Pacific Ocean are shown in Figure 6. The Ekman

component from the KPP solution is generally larger than that from the PP solution at the surface (Figure 6c). The geostrophic velocity relative to that at 1000 meter depth is computed from geopotential anomalies between 34°N and 36°N. The geopotential anomalies were calculated through the annual-mean distribution of temperature and salinity from the solutions by both schemes. Because the vertical eddy viscosity in the KPP solution is rather larger (Figure 4b), the Ekman spiral depth

$$D_E = \pi \left(\frac{2K_m}{|f|} \right)^{1/2} \quad (20)$$

is accordingly larger. Based on Figure 5, an average K_m of about $30\text{cm}^2\text{s}^{-1}$ can be found for the KPP solution. Checking with Table 2, D_E should be around 27 meters. This is consistent with the estimation from the vertical structure of Ekman velocity (Figure 6c). For the PP solution, K_m is very small except in the first level where a minimum value of $10\text{cm}^2\text{s}^{-1}$ is specified. Therefore, the Ekman layer from the PP solution is very shallow and almost no evident Ekman layer exists most of the time.

4.2 The Annual Cycle

Besides the mean state, the difference of K_m also results in a different annual cycle of both current and thermal structures.

a. Current

Figure 7 shows the vertical distribution of mean annual cycle of equatorial zonal currents taken at 140°W and 110°W during 1980-1991 from both observation (Yu and Schopf, 1997) and the twin 49-year (1945-1993) simulations. In general, both the phase and amplitude are comparable in both KPP and PP schemes. However, the depth of the maximum current amplitude in spring from the KPP scheme is closer to the TAO observation than the PP

scheme. In the extratropical region, the current structure also exhibits strong seasonal variability as shown in Figure 6d. In winter (January-March) when the wind is strongest, the zonal component of modeled Ekman current can reach 4cms^{-1} , while it is only about 1cms^{-1} in summer (July-September).

b. Temperature

Figure 8 shows the vertical distribution of zonally-averaged mean seasonal temperature anomalies in the whole Pacific basin for March and September. The seasonal temperature anomalies were calculated from the mean seasonal cycle of the last five years of the 30-year spin-up model integration. It can be seen that in the PP solution the mean seasonal temperature anomalies are mostly trapped near the surface. In contrast, in the KPP solution, the mean seasonal temperature anomalies are more realistically distributed in the upper ocean water column. A layer of 30-50 m deep with a uniform temperature can be found in the subtropics in both hemispheres. The improvement is rather significant, although it is still shallower in the KPP solution than in the Levitus climatology. It requires more extensive studies to ascertain to what extent the KPP scheme can be further improved, by adjusting the KPP parameters, using alternative surface forcing or interplaying the interaction between the KPP and GM schemes.

Figure 9 shows the zonally-averaged mean seasonal temperature anomalies in the mid-latitude (40°N) as a function of depth and month from the Levitus climatology and the differences between the two simulations and the Levitus climatology. For the KPP simulation, the difference is less than 1 degree most of the time except for the summer transition period when the monthly variation has the largest value (Fig. 9d). For the PP simulation, the seasonality is overestimated in the thin surface layer (about 20m) while underestimated in the interior and sandwiched in between with a thin layer of strong gradient, which is

obviously unrealistic (Fig. 9e). Besides leading to an erroneous ocean temperature, improper mixed-layer physics has also led to wrong sensible and latent heat fluxes, therefore, wrong upper ocean heat content. Figure 10 shows the seasonal anomalies of the vertically integrated heat content against the sea surface temperature averaged over the box region in the central North Pacific Ocean from 160°E to 160°W in longitude and from 30°N to 40°N in latitude. Note that the KPP solution is significantly better than the PP solution when compared with the Levitus climatology. The PP scheme underestimates the seasonal change of heat storage while overestimating the seasonal change of SST in this mid-latitude ocean region, which is consistent with a recent study of Stammer et al. (1996). In particular, the March temperature in the PP solution is 2 degrees colder than the Levitus observation, while the September temperature is over 1 degree warmer. The KPP scheme has resulted in a much larger heat storage capacity in the upper ocean than the PP scheme.

c. Boundary layer depth h

In the KPP scheme, the surface heat and fresh-water fluxes determine the surface buoyancy fluxes and surface wind forcing determine the surface momentum fluxes. Based on the turbulence similarity theory, these surface buoyancy and momentum fluxes should be able to penetrate into a depth where they first become stable relative to the local buoyancy and velocity. This boundary layer depth h is determined explicitly by calculating the bulk Richardson number relative to the surface according to Equation (18). Figure 12 shows the monthly-mean distribution of h for March. The distribution of h is strongly inhomogeneous, ranging from 10 m to more than 100 m. In the central tropical Pacific Ocean, h can change in the range of $30 < h < 100$ m. There is a distinct seasonal cycle for h , mainly due to the seasonal cycle of the surface heat fluxes. In general, in northern spring, h in the northern hemisphere is much deeper than that in the southern hemisphere. Especially in the Kuroshio

Current and its extension region and the central tropical Pacific region, the value of h can be as high as 100 m, implying that the surface momentum flux and buoyancy flux can penetrate as deep as 100 m before they reach stable condition. For comparison, the distribution of the mixed-layer depth (MLD) is also shown in Figure 11. Following Levitus et al. (1994), the MLD is defined as the depth where σ_t first exceeds its surface value by 0.125 kg m^{-3} . The MLD depends on the integrated performance of wind and also depends on the stability of the underlying water and on the heat and fresh-water balance through the surface. Overall, the distribution pattern of h is similar to that of MLD although MLD is generally deeper than h especially in the Kuroshio Current and its extension region and in the central Northeast Pacific region. The formation of the mixed layer is a complicated time-dependent process which is still not understood fully (Lukas and Lindstrom, 1991).

The seasonal cycle of h is primarily determined by the seasonal cycle of the surface fluxes, including both wind stirring and radiation fluxes. Figure 12 shows the monthly-mean value of $\ln(Ri_b)$ zonally averaged around the dateline for March and September. The monthly-mean values \bar{h} and MLD are also overlaid in Figure 12. Note that the MLD is much deeper than h especially in the season of winter when the wind stirring is strongest and the turbulent mixing is very intense within the OBL. The distribution of vertical eddy viscosity overlaid by the h and MLD is displayed for March and September in Figure 13, respectively. Within the OBL, the eddy viscosity K_m defined by Equation (17) is inhomogeneous in different regions. The vertical distribution is also nonuniform. The values at the bottom of the OBL are larger than those inside of the layer (Figure 5). Most of them change from $10 < K_m < 100.0 \text{ cm}^2 \text{ s}^{-1}$ and are seasonally dependent. Below the OBL, K_m is determined by Equation (13) and most values are in the range of $1.0 < K_m < 10.0 \text{ cm}^2 \text{ s}^{-1}$. The values below the OBL have been matched with those inside the OBL.

4.3 Interannual-to-Interdecadal Variability

While the tropical interannual variability associated with ENSO in the Pacific Ocean can be simulated reasonably well by the PP scheme (Philander et al., 1987; Philander, 1990), the extratropical interannual-to-interdecadal variability has not been well simulated with an OGCM (Philander, 1999, personal communication). A number of recent studies have reported the pronounced interannual-to-interdecadal variability in the extratropical Pacific Ocean (for recent reviews, see Mantua *et al.*, 1997, and Nakamura *et al.*, 1997). Although the cause of this variability is still a matter of debate, the spatial pattern of the decadal-to-interdecadal variability in the ocean has proven to be strongly 3-dimensional by analysing both SST and subsurface ocean thermal data (Zhang and Levitus, 1997). In particular, Deser et al. (1996) presented a detailed analysis of the vertical structure of seasonal thermal anomalies in the upper North Pacific Ocean during 1970-91, emphasizing the role of local interactions between the surface mixed layer and the thermocline in producing subsurface thermal anomalies. Figure 14 shows the time-depth structures of the seasonal temperature anomalies in the Kuroshio extension region as observed by Deser et al. (1996) and simulated by both the KPP and the PP experiments. Same as Deser et al. (1996), the seasonal temperature anomalies were calculated by removing the monthly-mean climatology from 1970 to 1991. The residuals were then averaged seasonally within the box region (34° - 42° N, 140° - 180° E). Note that, in the KPP simulation, the cold pulses beginning in 1981 are well simulated with comparable amplitudes and similar phases at the surface as well as in the deeper ocean. As observed, the surface-initiated cooling occurs nearly simultaneously within the upper 400 m and shows very little attenuation with depth. The deep penetration is well simulated by the KPP scheme in terms of both amplitude and phase. The -0.6°C contour line can reach as deep as 350-400 m where the permanent thermocline is located.

In sharp contrast, in the PP simulation, although the phase is relatively consistent with the observation, as expected, the depth of penetration is much shallower than the observation. Through detailed analysis, it is found that for the decadal-to-interdecadal time scale, the amplitudes simulated by both schemes are comparable at the surface, however, the amplitude inside the permanent thermocline in the KPP solution is much more realistic than in the PP solution. For the interannual time scale, the amplitudes from both the PP and KPP solutions are much weaker than the observed inside the permanent thermocline. It is not clear to what extent this lack of penetration in the KPP solution on interannual time scale can be attributed to the deficiency of the mixing scheme or to the poor quality of the interannual forcing. As described in Section 2.2, there is no interannual-to-interdecadal component of fresh-water flux in the surface forcing. Only the climatological fresh-water flux derived from COADS is used in the model salinity equation. This issue requires further investigation.

In short, for the decadal-to-interdecadal time scale, the PP scheme seriously lacks the capability of penetrating this low-frequency thermal anomaly into the permanent thermocline, while the KPP scheme has a reasonable good skill in penetrating this anomaly into the permanent thermocline. For the interannual time scale, both schemes seem to fail in producing the thermal anomaly effectively below the mixed-layer.

5. Discussions and Summary

In this paper we have studied the impact of two different vertical mixing schemes on the solution of a Pacific OGCM. In the conventional PP scheme, the vertical eddy viscosity and diffusivity are determined based on local vertical gradients of density and velocity. In contrast, the KPP scheme includes nonlocal processes and determines the vertical profiles of eddy viscosity and diffusivity based on a diagnosed boundary-layer depth and a turbulent

velocity scale. The boundary-layer depth is determined through the requirement that surface momentum and buoyancy fluxes should penetrate to a depth where they become stable relative to the local velocity and buoyancy. The turbulent velocity scale is a function of surface wind forcing, buoyancy forcing, and the boundary-layer depth. It also incorporates a smooth transition to the parameterization of interior vertical mixing.

The PP and KPP schemes have been compared using two 49-year (1945-1993) simulation experiments forced by real-time, monthly-mean wind stresses and heat fluxes derived from COADS. The comparison is made in both tropical and extratropical regions for the annual-mean state, annual cycle, and interannual-to-interdecadal variability. Overall, the KPP scheme has produced more realistic simulations of the upper ocean thermal structures. In the tropics, the KPP vertical mixing scheme produces more realistic thermal structures than the PP scheme. As an example, the cold tongue in the KPP solution is less cold than in the PP solution. In the extratropics, however, the KPP scheme is significantly better in simulating the temperature anomalies and the upper ocean heat storage when compared with observations.

Both the mean state and the seasonal cycle of current structures have also been analyzed. It is found that the core of equatorial Undercurrent in the KPP solution has comparable amplitude but about 20 meter deeper than in the PP solution and closer to TAO observations. In the middle latitude, the Ekman spiral depth in the KPP solution is about 20-30 m deep by investigating the current structures in the central North Pacific Ocean region. For the PP solution, the Ekman layer is either very shallow or almost does not exist. The improvement in both the tropics and the extratropics can be explained by that in the KPP scheme more realistic profiles of vertical eddy viscosity and diffusivity have been parameterized than in the PP scheme.

In conclusion, the KPP scheme works well in both the tropics and the extra-tropics, while the PP scheme appears to be applicable only in the tropics where the shear-dependent instability dominates in the turbulent mixing. Another difference between the two schemes lies in the treatment of convection. For the PP scheme, an *ad hoc* convection scheme is used whenever the $R_{ig} < 0$. This scheme sets eddy viscosity and diffusivity to very large values. For the KPP scheme, on the other hand, the convection process is explicitly treated through calculating the turbulent velocity scale and adding the contribution of both turbulent velocity shear and entrainment flux. In comparison to the high-order turbulence closure schemes, the advantage of the KPP scheme is its relative insensitivity to vertical resolution. Given the correct surface forcing and advective transports, it will properly distribute properties in the vertical according to the empirical functions determined from measurements. From a computational point of view, the addition of the KPP scheme increases only about 10% of the computing time. It is, thus, more efficient than high-order turbulence closure schemes, which requires 50% or more computational time (Rosati and Miyakoda, 1988). The success of the KPP scheme can be attributed to: (1) a realistic prediction of an ocean boundary layer depth through a bulk Richardson number; (2) an explicit assumption for the shape of the distribution of the turbulent coefficients; (3) a nonlocal transport dependent on the surface fluxes and the boundary layer depth; and (4) a shear-dependent mixing region below the boundary layer. Among them, the explicit assumption for the shape of the distribution of the turbulent coefficients is the key. The nonlocal transport represents the important processes of turbulent mixing in the boundary layer where there are various coherent structures, such as buoyant vertical plumes, Langmuir circulation, Kelvin-Helmholtz waves, and internal gravity waves. The significance of this nonlocal transport term in different situations remains to be determined.

Although the KPP scheme has made significant improvement in simulating the vertical distribution of thermal and kinetic energy, there are still room for improvement. The penetration depth is not as deep as observed, especially for interannual variability (although it may be due to the poor quality of the interannual forcing). Besides further adjusting the interior mixing parameters (Large, 1999, personal communication), it is expected that the KPP solutions can be further improved by more accurate representation of the heat and fresh water fluxes. One of the future studies with the nonlocal KPP scheme should focus on using synoptic forcing (with a high-frequency component, such as diurnal cycle) to drive the ocean boundary layer. In this case, the turbulence will be developed fully inside the boundary layer and the physics of turbulence similarity theory might be more effective in explaining the real situation. The sensitivity of the KPP scheme to salinity and fresh-water flux and its potential impact on simulating the low-frequency thermal variability also requires careful investigation.

According to recent intercomparison studies (Stammer et al., 1996), there are discrepancies between the OGCM simulation using the PP scheme and observations in terms of both large-scale mean circulation and its variability, especially in the extra-tropics. It has been shown that improvements in external surface forcing fields, including wind-stress fields and sea surface heat and fresh water fluxes, can lead to a significant improvement in their overall agreement (Fu and Smith, 1996; Large et al., 1997). It is our belief that improved boundary layer physics such as provided by the KPP scheme should produce further improvement to the OGCM simulations. Furthermore, an OGCM with an efficient, physically-based boundary-layer and interior vertical mixing mechanism such as the KPP scheme should enable the construction of better coupled atmospheric-ocean models for the study of natural climate variability and anthropogenic climate changes. The processes and mechanisms for the cli-

mate regime shift in the North Pacific Ocean around 1976-77 and the exchange between the extratropics and the tropics can be investigated through models with this improved vertical mixing scheme.

Acknowledgements. The research described in this paper was carried out, in part, by the Jet Propulsion Laboratory (JPL), California Institute of Technology, under contract with National Aeronautics and Space Administration. Support from the JPL Director's Research and Development Fund is acknowledged. We'd like to thank Dr. Clara Deser and Michael S. Timlin for providing us the XBTs data used in Figure 14 and Arlindo M. da Silva at Goddard Space Flight Center for providing the COADS data. Computations were performed on the Cray J90 through the JPL Supercomputing Project.

APPENDIX A

The Turbulent Velocity Scales in the Nonlocal KPP Scheme

The turbulent velocity scale of Eq. (17) depends primarily on the relative height d/h (h is the OBL depth) and the stability within the OBL (Högström, 1988; Holtslag and Boville, 1993; Large et al., 1994). Here, stability is defined with respect to the surface active heat flux $\overline{wt_0}$, or equivalently with the ratio h/L (L being the Monin-Obukhov length scale). Secondly, the velocity scales are also dependent on the specific quantity of interest. We will assume that the velocity scales for mixing of scalars, such as temperature and salinity, are equally denoted by w_t . For the momentum component, the velocity scale is different and denoted by w_m . The specification of w_t and w_m is given in details by Large et al. (1994).

For stable ($\overline{wt_0} < 0$ or $h/L > 0$) and neutral surface conditions ($\overline{wt_0} = 0$ or $h/L = 0$), the velocity scale for passive tracer is

$$w_t = \frac{u_*}{\phi_t}, \quad (21)$$

where u_* is the friction velocity defined by

$$u_*^2 = (\overline{wu_0^2} + \overline{wv_0^2})^{1/2}. \quad (22)$$

Meanwhile ϕ_t is the dimensionless vertical temperature gradient given by

$$\phi_t = 1 + 5 \frac{d}{L} \quad (23)$$

for $\frac{d}{L} \geq 0$. L is the Monin-Obukhov length and defined by

$$L = \frac{-u_*^3}{k(\alpha g)\overline{wt_0}} \quad (24)$$

where $k = 0.4$ is called von Karman's constant, α thermodynamic expansion coefficient, g is the gravitational acceleration. In stable conditions, the exchange coefficients for heat and

momentum are often found to be similar (Large et al, 1994). Therefore, we use in the model $w_m = w_t$.

For unstable conditions ($\overline{wt_0} > 0$ or $h/L < 0$), the forms w_t and w_m differ from each other and the difference could be dramatic for strong convective situation. In general, for unstable profile, the OBL can be treated as two layers: thin surface layer and deeper boundary layer. For the thin surface layer (usually $\frac{d}{L} \geq -1.0$ for heat), w_t is given by Eq. (21) and

$$\phi_t = (1 - 16d/L)^{-1/2}. \quad (25)$$

Similarly w_m is written as

$$w_m = \frac{u_*}{\phi_m} \quad (d/L \leq 1.0), \quad (26)$$

where ϕ_m is the dimensionless current speed gradient given by

$$\phi_m = (1 - 16d/L)^{-1/4} \quad (d/L \leq -0.2). \quad (27)$$

For the deeper layer, ϕ_t and ϕ_m can be written as

$$\phi_t = (-28.86 - 98.96d/L)^{-1/3} \quad (d/L \leq -1.0), \quad (28)$$

$$\phi_m = (1.26 - 8.38d/L)^{-1/3} \quad (d/L \leq -0.2). \quad (29)$$

All these unstable forms match the stable functions at $d/L = 0$ (neutral state) and are based upon the available data (Högström, 1988). As you can see from Large et al. (1994, Figure B1), for all $d/L < 0$, $\phi_m > \phi_t$, therefore, $w_m < w_t$, convection always mixes scalar tracers, including buoyancy, more efficiently than momentum.

For the pure convective situation when u_* approaches zero, the ocean boundary layer turbulence is well behaved because it becomes dependent on a convective velocity scale defined by

$$w_* = (-B_f h)^{1/3}. \quad (30)$$

Combining all these equations leads to

$$w_x = k(a_x u_*^3 + c_x k \sigma w_*^3)^{1/3}. \quad (31)$$

For the convective limit, the relation becomes as

$$w_x = k(c_x k \sigma)^{1/3} w_*. \quad (32)$$

APPENDIX B

Turbulent Velocity Shear

The destabilizing shear term of Eq. (18), besides having the magnitude squared of the vector mean velocity difference from (U_r, V_r) , also includes another term $V_t(d)$, called turbulent velocity shear (strictly speaking, equal to V_t/d), which is often not negligible and is most important in pure convection and other situations of little or no mean shear. Therefore this term needs to be parameterized. First of all, it should increase with the turbulent velocity scale and decrease with stratification $\partial_z B = N^2$, where N is the local buoyancy frequency. These dependencies and dimensional considerations suggest that

$$\left(\frac{V_t}{d}\right)^2 \propto \frac{N w_x}{d}. \quad (33)$$

In order to determine the detailed form of V_t , a special case of pure convection ($u_* = 0$, $B_f < 0$) and no mean shear with a well-mixed layer of buoyancy B_r eroding into a layer of constant stratification, N , is considered. As an empirical rule of convection, the ratio of entrainment flux $\overline{wb_e}$ and surface buoyancy flux $\overline{wb_o}$ in this case $\frac{\overline{wb_e}}{\overline{wb_o}} = \beta_T$ (Figure 1 at Large et al., 1994). The convection rule, plus relations Eqs. (16), (17) and the assumption of $\gamma_b \ll N^2$. Notice that the numerator of Eq. (18) at $d = h$ becomes $h(h - h_e)N^2$. So we have $G(\frac{h_e}{h}) = \frac{(h-h_e)^2}{h^2}$ and $N(h_e) = N/C_v$, constant $1 < C_v < 2$ ($C_v = 1.6$ in our simulation, which accounts for some smoothing of buoyancy profile at h_e caused by mixing).

Eliminating h_e , we can get

$$V_t^2(h) = \frac{C_v(-\beta_T)^{1/2}}{R_{ic}k^{2/3}}(c_s\varepsilon)^{-1/6}hNw_*. \quad (34)$$

Using the scalar (32) to go from the pure convective to the general case gives

$$V_t^2(d) = \frac{C_v(-\beta_T)^{1/2}}{R_{ic}k^2}(c_s\varepsilon)^{-1/2}dNw_t. \quad (35)$$

Without the V_t^2 term in Eq. (18), cases of larger N at the bottom of the boundary layer would tend to have smaller entrainment fluxes because the larger buoyancy gradient is insufficient to compensate for the very much smaller diffusivity resulting from the smaller h . However, with this term the larger N gives a larger h from Eq. (18), and hence for a fixed h_e the smaller h_e/h and the larger h increase the diffusivity in Eq. (17) just enough to keep the entrainment flux independent of N . Although the ratio of this flux to the surface buoyancy flux will be a constant $-\beta_T$ in the convective limit, it will depend on u_* in forced convection.

APPENDIX C

Nonlocal Transport Term γ_x

The nonlocal transport term in Eq. (16), γ_x , which represents nonlocal impact of the large-scale turbulence mixing, is non-zero only for scalar tracers under unstable forcing. In such cases, as was suggested by Large et al. (1994), it has been successfully parameterized by Mailbôt and Benoit (1982) as

$$\gamma_x = C \frac{\overline{wx_o}}{w_*h} \quad (36)$$

where $w_* = (-B_f h)^{1/3}$ is called convective velocity scale, $C = 10$, a constant in a highly convective situation. This nonlocal transport represents those important processes of turbulent mixing in the boundary layer where there are various coherent structures, such as

buoyant vertical plumes, Langmuir circulation, Kelvin-Helmholtz waves and internal gravity waves. The significance of this nonlocal transport term in different situations remains to be determined.

Table 1. Vertical grid size and depth used in the NCOM

Level	Grid Size (m)	Depth (m)
1	10.00	10.00
2	10.00	20.00
3	10.00	30.00
4	10.00	40.00
5	10.00	50.00
6	10.05	60.05
7	10.17	70.22
8	10.44	80.66
9	11.05	91.71
10	12.33	104.04
11	14.87	118.91
12	19.70	138.61
13	28.38	166.99
14	43.20	210.19
15	67.18	277.37
16	103.92	381.29
17	157.13	538.42
18	229.85	768.27
19	323.33	1091.60
20	436.10	1527.70
21	562.20	2089.90
22	693.30	2783.20
23	816.10	3599.30
24	917.00	4516.30
25	983.70	5500.00

Table 2. Ekman Spiral Depth against Vertical Viscosity (Latitude: 35°N)

$D_E : m$	$K_m : cm^2 s^{-1}$
4.86	1
15.38	10
21.75	20
26.64	30
30.76	40
34.40	50
48.64	100
108.77	500
153.82	1000

REFERENCES

- Ayotte, K. W., P. P. Sullivan, A. Andren, S. C. Doney, A. M. Holtslag, W. G. Large, J. C. McWilliams, C.-H. Moeng, M. J. Otte, J. J. Tribbia and J. C. Wyngaard, 1996: An evaluation of neutral and convective planetary boundary-layer parameterizations relative to large eddy simulations. *Bound.-Layer Meteor.*, **79**, 131-175.
- Barnier, B., L. Siefridt, and P. Marchesiello, 1995: Thermal forcing for a global ocean circulation model using a 3-year climatology of ECMWF analysis. *J. of Mar. Sci.*, **6**, 363-380.
- Blanke, B. and P. Delecluse, 1993: Variability of the tropical Atlantic Ocean simulated by a general circulation model with two different mixed-layer physics. *J. Phys. Oceanogr.*, **23**, 1363-1388.
- Bryan, K. and L. J. Lewis, 1979: A water mass model of the world ocean. *J. Geophys. Res.*, **84**, 2503-2514.
- Bryan, K., 1969: A numerical method for the study of the world ocean. *J. Comput. Phys.*, **4**, 347-376.
- Chen, D., L. M. Rothstein and A. J. Busalacchi, 1994: A hybrid vertical mixing scheme and its application to tropical ocean models. *J. Phys. Oceanogr.*, **24**, 2157-2179.
- Cox, M. D., 1984: A primitive equation, 3-dimensional model of the ocean. *GFDL Ocean Group Tech. Rep.*, **1**, 1-143.
- Crawford, W. R. and T. R. Osborn, 1979: Microstructure measurements in the Atlantic Equatorial Undercurrent during GATE. *Deep-Sea Res.*, **26** (Supp. II), 285-308.

- da Silva, A. M., C. C. Young and S. Levitus, 1994: Atlas of surface marine data 1994, NOAA Atlas NESDIS, *US Dept. of Commerce*.
- Deser, C., M. A. Alexander and M. S. Timlin, 1996: Upper ocean thermal variations in the North Pacific during 1970-1991. *J. Climate*, **9**, 1840-1855.
- Fu, L.-L., and R. D. Smith, 1996: Global ocean circulation from satellite altimetry and high-resolution computer simulation. *Bull. Amer. Meteorolog. Soc.*, **77(11)**, 2625-2627.
- Garwood, R. W. , 1977: An oceanic mixed layer model capable of simulating cyclic states. *J. Phys. Oceanogr.*, **7**, 455-467.
- Gent, P. R., and J. C. McWilliams, 1990: Isopycnal mixing in ocean circulation models. *J. Phys. Oceanogr.*, **20**, 150-155.
- Gent, P. R., F. O. Bryan, G. Danabasoglu, S. C. Doney, W. R. Holland, W. G. Large, and J. C. McWilliams, 1998: The NCAR climate system model global ocean component. *J. Climate*, **11(6)**, 1287-1306.
- Gnanadesikan, A., and R. A. Weller, 1995: Structure and instability of the Ekman spiral in the presence of surface gravity waves. *J. Phys. Oceanogr.*, **25**, 3148-3171.
- Haidvogel, D. B., and A. Beckmann, 1999: Numerical ocean circulation modeling, Imperial College Press, 318pp.
- Halpern, D., Y. Chao, C. C. Ma and C. R. Mechoso, 1995: Comparison of tropical Pacific temperature and current simulations with two vertical mixing schemes embedded in

- an ocean general circulation model and reference to observations. *J. Geophys. Res.*, **100**, 2515-2523.
- Högström, U., 1988: Non-dimensional wind and temperature profiles in the atmospheric surface layer: A re-evaluation. *Boundary Layer Meteorol.*, **42**, 55-78.
- Holtslag, A. A., and B. A. Boville, 1993: Local versus nonlocal boundary-layer diffusion in a global climate model. *J. Climate*, **6**(10), 1825-1842.
- Kantha, L. H. and C. A. Clayson, 1994: An improved mixed layer model for geophysical applications. *J. Geophys. Res.*, **99**(C12), 25235-25266.
- Kraus, E. B. and J. S. Turner, 1967: A one-dimensional model of the seasonal thermocline, II, The general theory and its consequences. *Tellus*, **19**, 98-105.
- Large, W. G., and S. Pond, 1981: Open ocean momentum flux measurements in moderate to strong winds. *J. Phys. Oceanogr.*, **11**, 324-336.
- Large, W. G., J. C. McWilliams and S. C. Doney, 1994: Oceanic vertical mixing: a review and a model with a nonlocal boundary layer parameterization. *Rev. Geophys.*, **32**, 363-403.
- Large, W. G., G. Danabasoglu, S. C. Doney and J. C. McWilliams, 1997: Sensitivity to surface forcing and boundary layer mixing in a global ocean model: annual-mean climatology. *J. Phys. Oceanogr.*, **27**, 2418-2447.
- Large, W. G. and P. R. Gent, 1999: Validation of Vertical Mixing in an Equatorial Ocean Model Using Large Eddy Simulations and Observations. *J. Phys. Oceanogr.*, **29**, 449-464.

- Levitus, S., R. Burgett, T. Boyer, 1994: World Ocean Atlas, 1994, Vol.,3: Salinity and Vol.4,: Temperature, NOAA Atlas NESDIS 3 4. *US Dept. of Commerce*.
- Lukas, R. and E. Lindstrom, 1991: The mixed layer of the western equatorial Pacific Ocean. *J. Geophys. Res.*, **96** supplement, 3343-3357.
- Mailhôt, J. and R. Benoit, 1982: A finite-element model of the atmospheric boundary layer suitable for use with numerical weather prediction models. *J. Atmos. Sci.*, **39**, 2249-2266.
- Mantua, J. N., S. R. Hare, Y. Zhang, J. M. Wallace, and R. C. Francis, 1997: A Pacific interdecadal climate oscillation with impacts on salmon production. *Bull. Amer. Meteor. Soc.*, **78**, 1069-1080.
- McWilliams, J. C., P. P. Sullivan, and C. H. Moeng, 1997: Langmiur turbulence in the ocean. *J. Fluid Mech.*, **334**, 1-30.
- Mellor, G. L. and T. Yamada, 1982: Development of a turbulence closure model for geophysical fluid problems. *Rev. Geophys.*, **20**, 851-872.
- Nakamura, H., G. Lin, and T. Yamagata, 1997: Decadal climate variability in the North Pacific during recent decades. *Bull. Amer. Meteor. Soc.*, **78**, 2215-2225.
- Niiler, P. P. and his colleagues at Scripps Institution of Oceanography, 1995: Comparison of TOGA tropical Pacific Ocean model simulations with the WOCE/TOGA surface velocity programme drifter data set. *World Climate Research Programme*, 1-156.
- O'Brien, J. J., 1970: A note on the vertical structure of the eddy exchange coefficient in the planetary boundary layer. *J. Atmos. Sci.*, **27**, 1213-1215.

- Osborn, T. R. and L. E. Bolodean, 1980: Temperature microstructure in the Atlantic Equatorial Undercurrent. *J. Phys. Oceanogr.*, **10**, 66-82.
- Pacanowski, R., and S. G. H. Philander, 1981: Parameterization of vertical mixing in numerical models of tropical oceans. *J. Phys. Oceanogr.*, **11**, 1443-1451.
- Pacanowski, R. C., K. Dixon, and A. Rosati, 1991: The GFDL modular ocean model user guide, The GFDL Ocean Group Technical Report No. 2, *Geophysical Fluid Dynamics Laboratory, Princeton, USA*.
- Paulson, C. A. and J. J. Simpson, 1977: Irradiance measurements in the upper ocean. *J. Phys. Oceanogr.*, **7**, 952-967.
- Peters, H., M. C. Gregg and J. M. Toole, 1988: On the parameterization of equatorial turbulence. *J. Geophys. Res.*, **93**, 1199-1211.
- Philander, S. G. H., W. Hurlin, and A. D. Seigel, 1987: A model of the seasonal cycle in the tropical Pacific Ocean. *J. Phys. Oceanogr.*, **17**, 1986-2002.
- Philander, S. G. H., 1990: El Nino, La Nina and the Southern Oscillation. *Academia Press*, 1-293.
- Price, J. F., R. A. Weller and R. Pinkel, 1986: Diurnal cycling: Observations and models of the upper ocean response to diurnal heating, cooling and wind mixing. *J. Geophys. Res.*, **91**, 8411-8427.
- Robinson, A. R., 1966: An investigation into the wind as the cause of the Equatorial Undercurrent. *J. Mar. Res.*, **24**, 179-191.

Figure Captions

Figure 1. The mean vertical profiles of K_m calculated from Equation (13) in PP (dotted line) and Equation (17) in KPP schemes (solid line) on the equator at 165°E (a), 140°W (b) and 110°W (c), respectively. Unit is in $cm^2 s^{-1}$.

Figure 2. The vertical profiles of long-term mean zonal current from TOGA (+), KPP (solid lines) and PP (dotted lines) along the equator at 165°E, 140°W and 110°W, respectively. Unit is in $cm s^{-1}$.

Figure 3. Annual-mean temperature along the equator from Levitus climatology (a), KPP simulation (b), PP simulation (c), and the difference between Levitus climatology and KPP (d) and PP (e) simulations. Unit is in °C.

Figure 4. Annual-mean SST from Levitus climatology (a), KPP simulation (b), PP simulation (c), and the differences between Levitus climatology and KPP (d) and PP (e) simulations. Unit is in °C.

Figure 5. The mean vertical profile of K_m calculated from Equation (13) in PP (dotted line) and Equation (17) in KPP schemes (solid line) in the central North Pacific Ocean region from 176°E to 176°W in longitude and from 34°N to 36°N in latitude. Unit is in $cm^2 s^{-1}$.

Figure 6. The vertical profiles of the annual-mean total zonal velocity (a), the annual-mean geostrophic zonal velocity (b), the annual-mean zonal Ekman velocity (c) and two different seasonal mean Ekman velocities (d and e) averaged in the same region as in Figure 5. The geostrophic velocity is computed by calculating the geopotential anomalies between 34°N and 36°N and is relative to level-19 which is between 768 and 1092 meter depth. Unit is in $cm s^{-1}$. Same as in Figure 4, PP (dotted) and KPP (solid). Note the different vertical scale in (b).

Figure 7. Annual cycles of equatorial zonal currents from TAO observations taken at

140°W and 110°W (upper) and from KPP (middle) and PP (lower) simulations. TAO observation is from Yu and Schopf (1997). Unit is in $cm\ s^{-1}$.

Figure 8. Zonally-averaged temperature anomalies (with annual-mean values removed) as a function of depth and latitude from Levitus climatology (top), KPP solution (middle) and PP solution (bottom) for March and September. Contour interval is $0.5^{\circ}C$.

Figure 9. Zonally-averaged temperature anomalies as in Figure 8 at $40^{\circ}N$ as a function of time and depth from Levitus climatology (a), KPP (b) and PP (c). The differences between the simulations and Levitus climatology are also shown (d and e). Contour interval is $0.5^{\circ}C$.

Figure 10. Heat content anomalies as a function of sea surface temperature from Levitus climatology (solid line), KPP solution (dashed line) and PP solution (dotted line) averaged over a box region from $160^{\circ}E$ to $160^{\circ}W$ in longitude and from $25^{\circ}N$ to $40^{\circ}N$ in latitude. The heat content anomaly is integrated up to 277 m and averaged over the box region with a unit of $^{\circ}C\ m$. The number (1, 2, ..., 12) represent the month of January, February, ..., December.

Figure 11. The distribution of monthly-mean boundary layer depth h (above) and monthly-mean mixed-layer depth (below) from the KPP solution at March averaged between 1971 and 1990. Contour interval is 20 m. The mixed-layer depth is defined as the depth where σ_t first exceeds its surface value by $0.125\ kg\ m^{-3}$. The rectangular box region (below) is defined as the Kuroshio Current Extension region used in Figure 14.

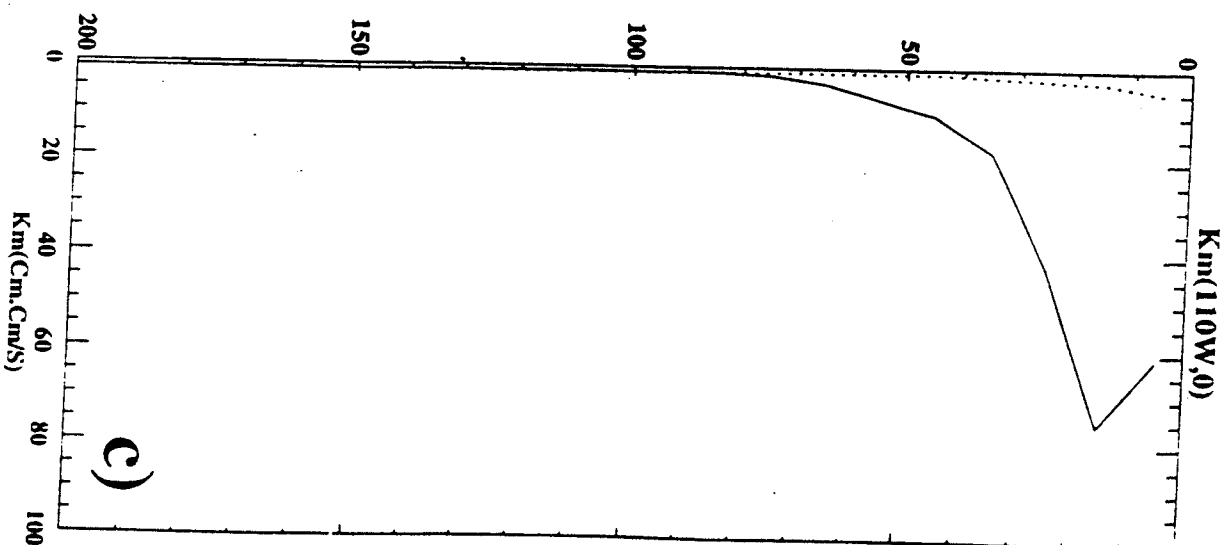
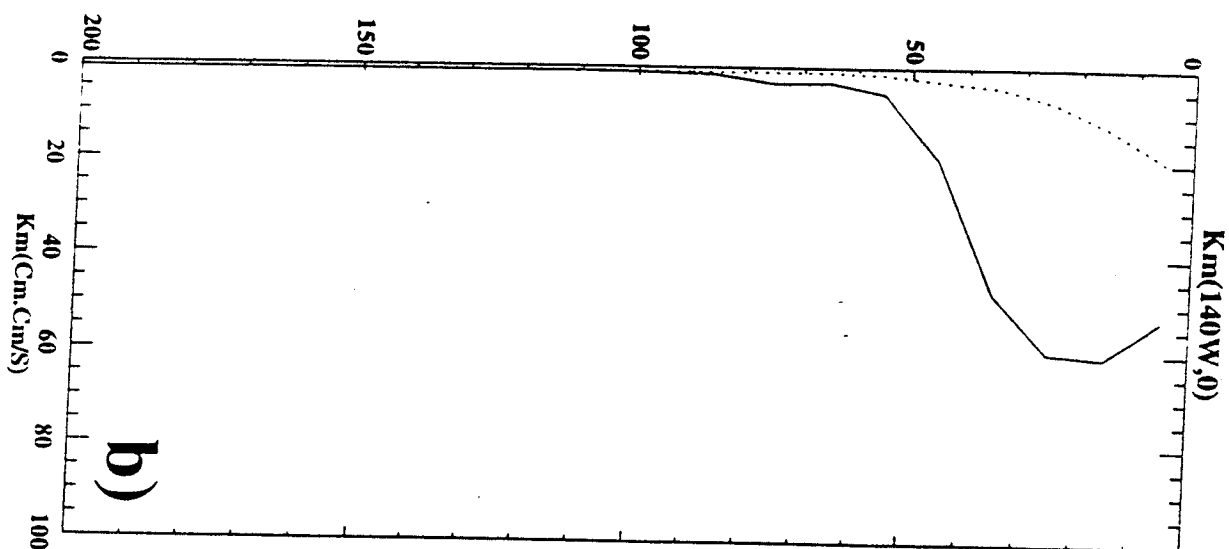
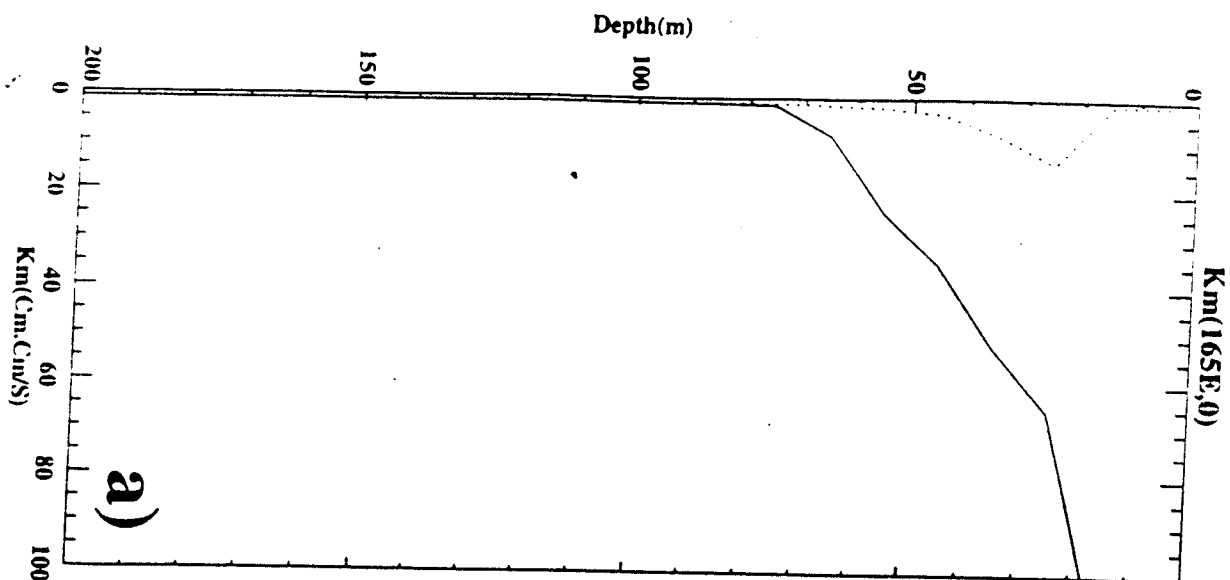
Figure 12. Monthly-mean bulk Richardson number (in natural logarithm) as a function of depth and latitude for March and September. The bold solid lines represent monthly-mean boundary-layer depth and the bold dotted lines represent the monthly-mean mixed-layer depth.

Figure 13. Monthly-mean vertical eddy viscosity calculated from KPP scheme and averaged between 1971 and 1990 as a function of depth and latitude for March and September

at dateline. The bold solid lines represent the monthly-mean boundary-layer depth and the bold dotted lines represent the monthly-mean mixed-layer depth.

Figure 14. Monthly-mean temperature anomalies as a function of depth and time from Deser et al. (1996) observation (top), KPP simulation (middle), and PP simulation (bottom). The monthly-mean temperature anomalies are calculated by averaging the value in the Kuroshio Current Extension (KCE) region ($34^{\circ}N - 42^{\circ}N$, $140^{\circ}E-180^{\circ}E$, see Figure 11). Contour interval is $0.2^{\circ}C$, and dark shaded when anomalies greater than $0.4^{\circ}C$ and grey shaded when anomalies between $-0.4^{\circ}C$ and $0.4^{\circ}C$. For Deser et al. (1996) observation data, there is a gap in the middle of 1970s.

Fig. 1



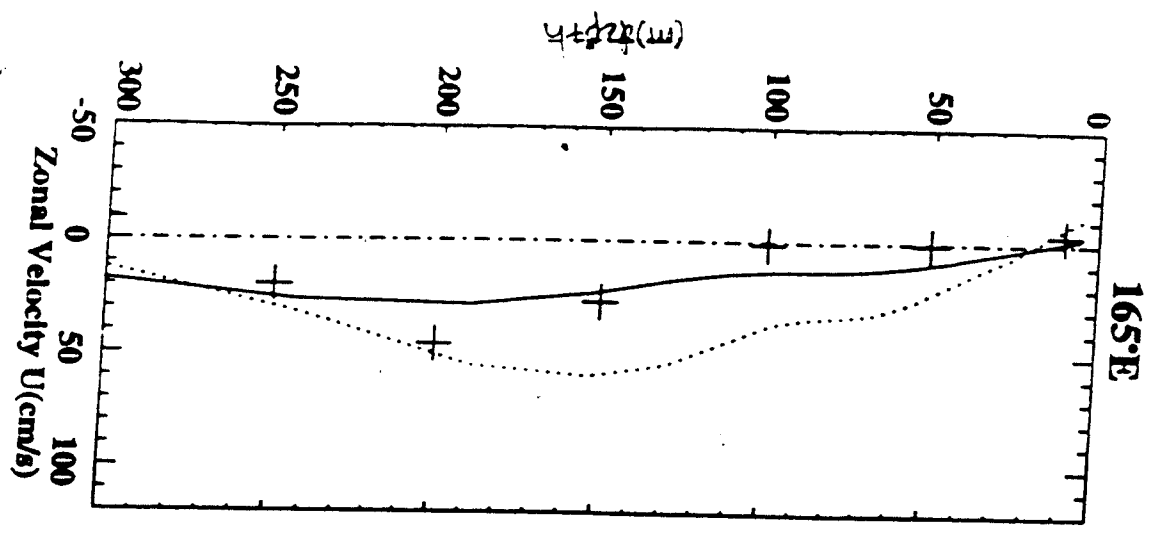
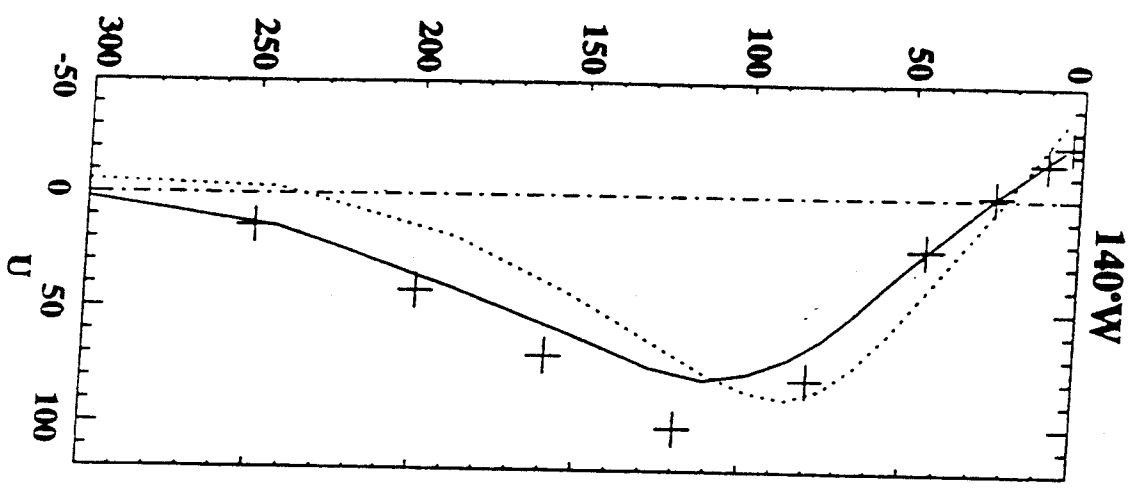
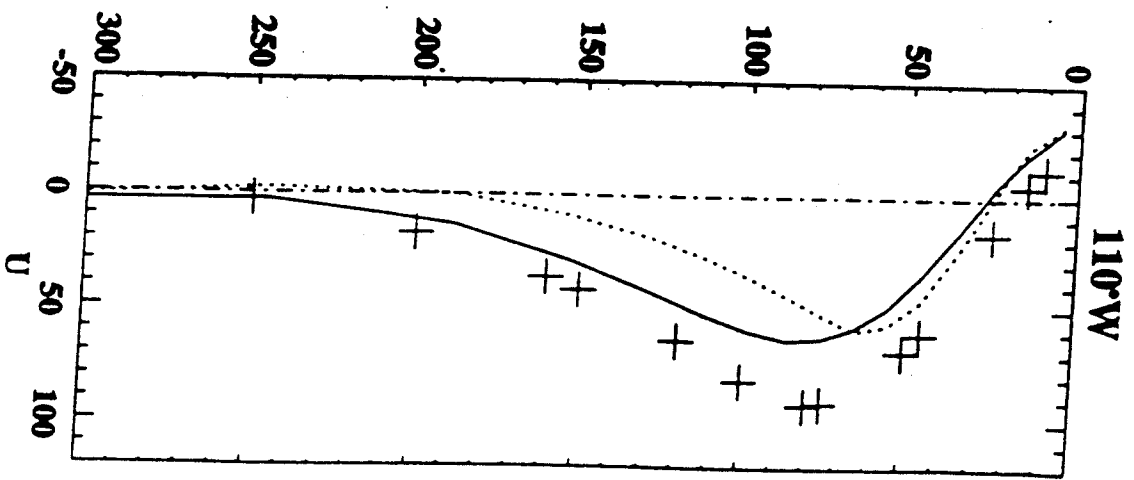
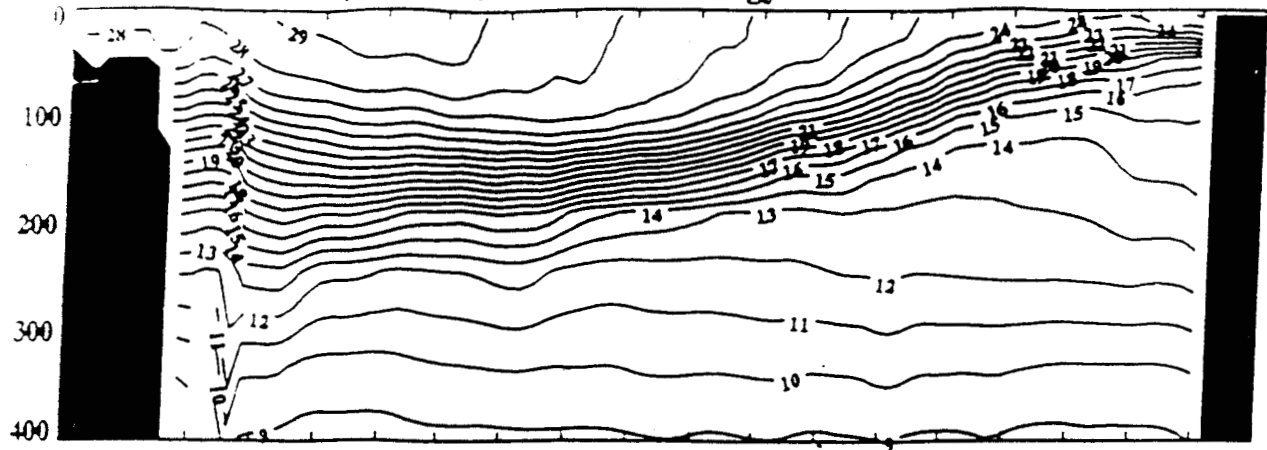
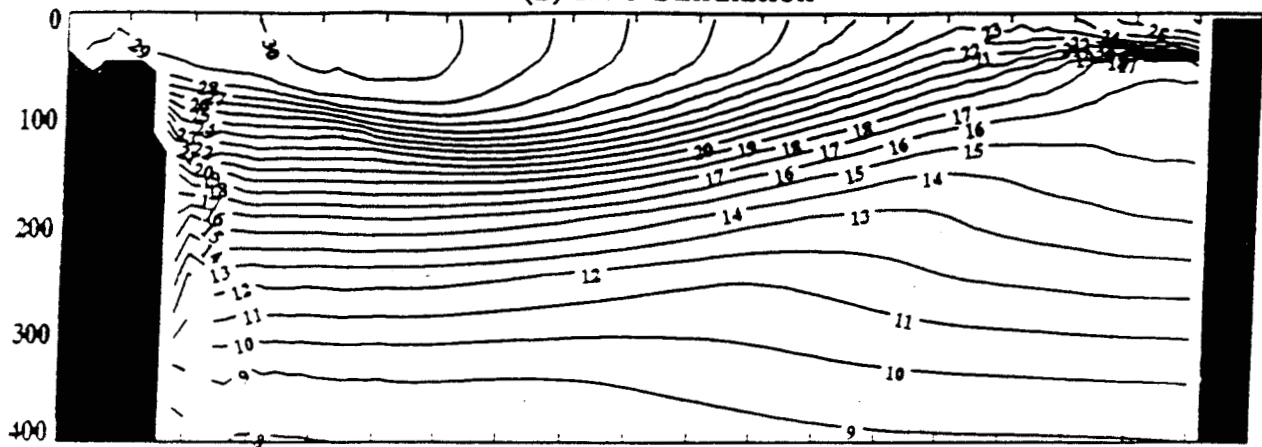


Fig. 2

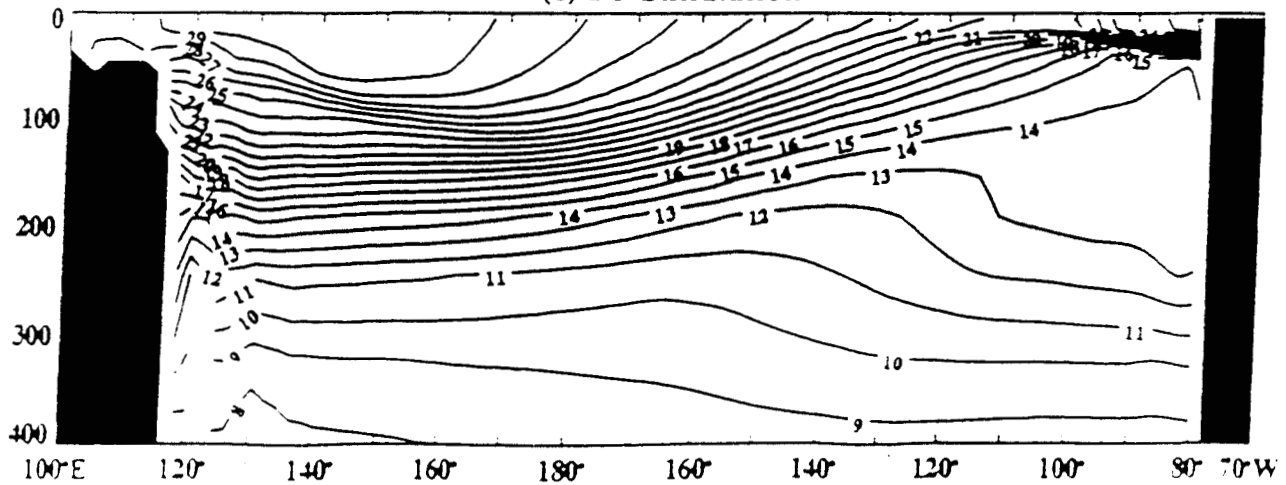
(a) Annual Mean Climatology of Levitus SST

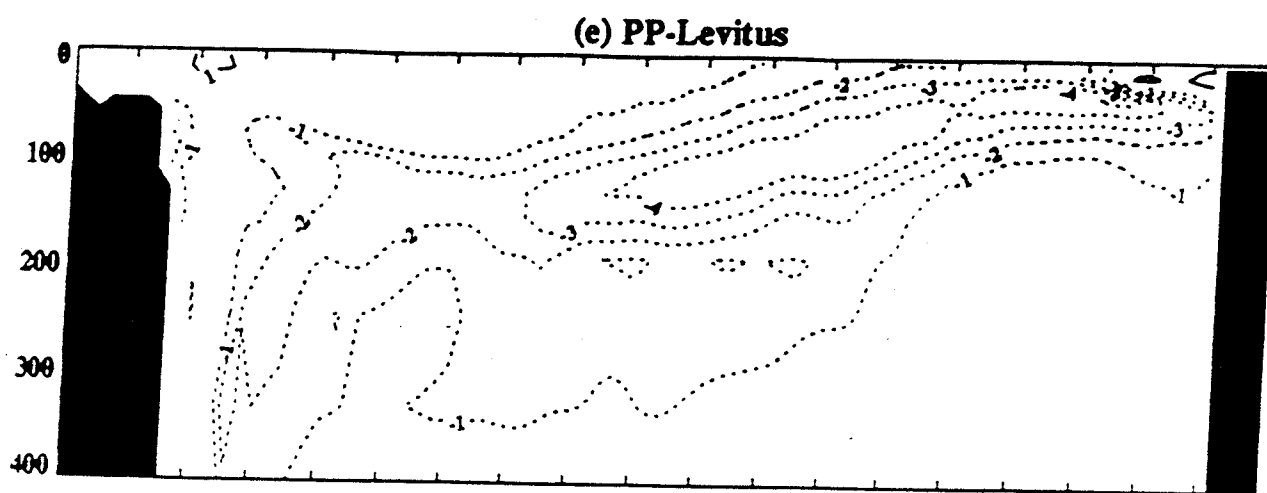
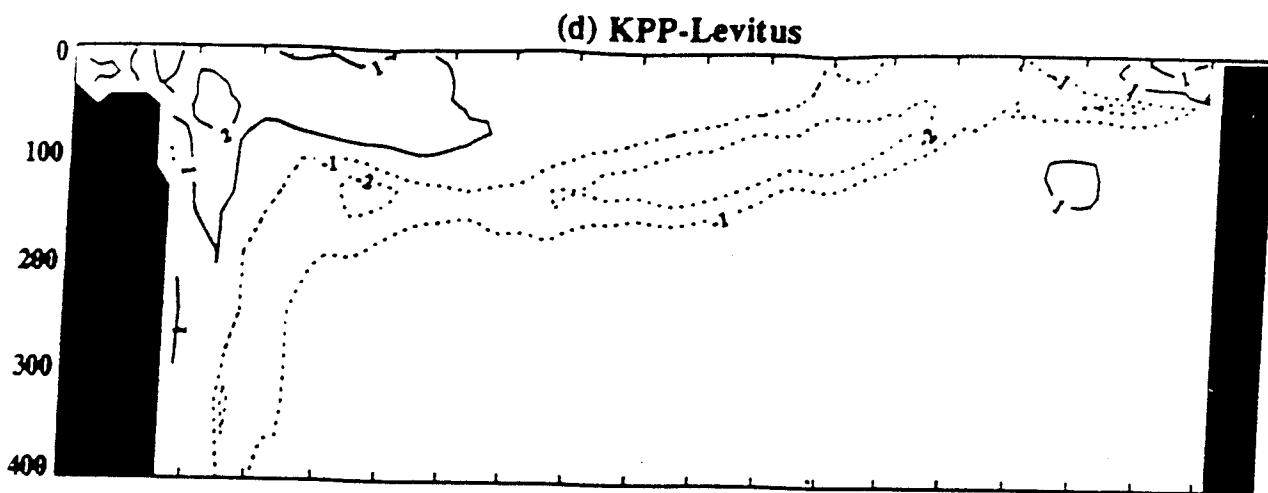


(b) KPP Simulation

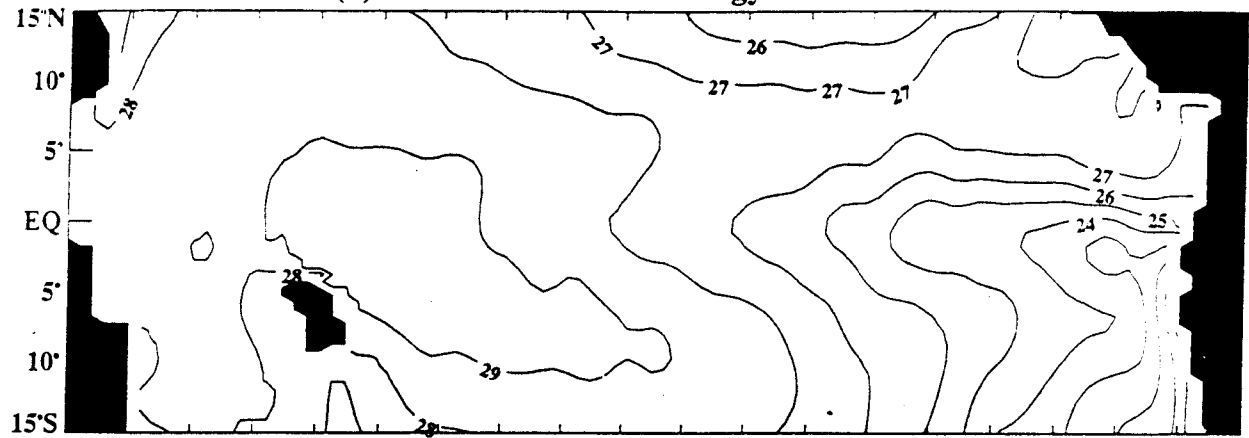


(c) PP Simulation

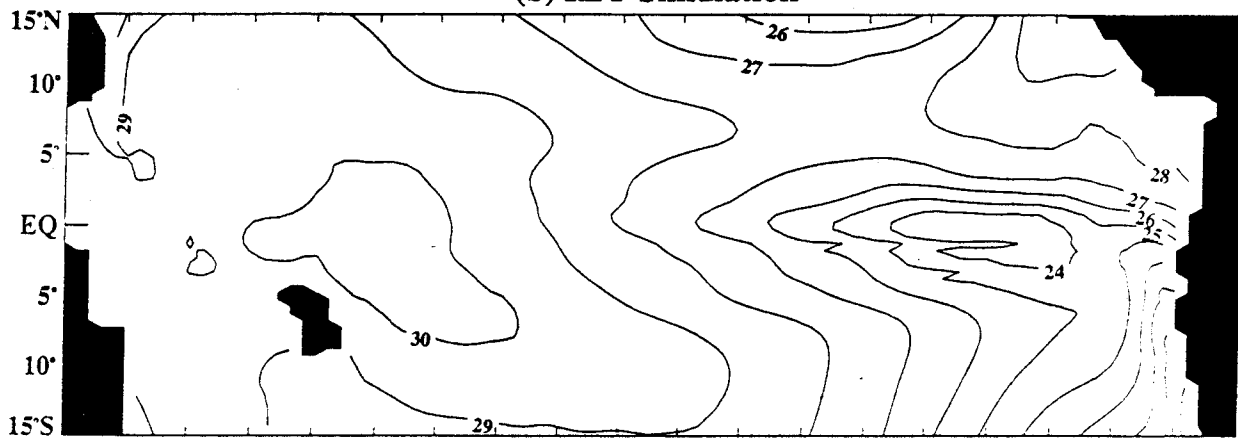




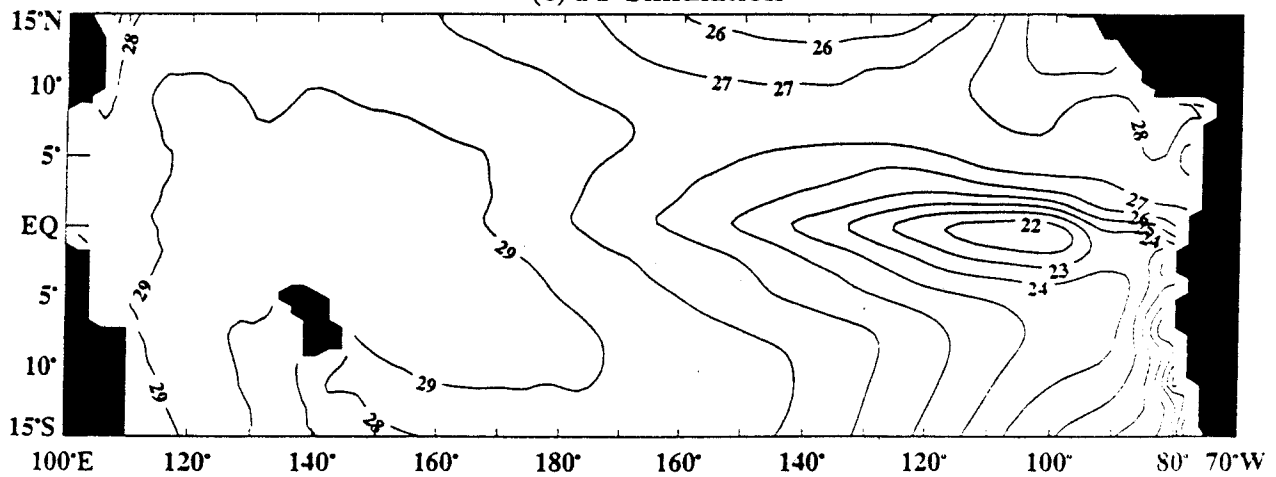
(a) Annual Mean Climatology of Levitus SST



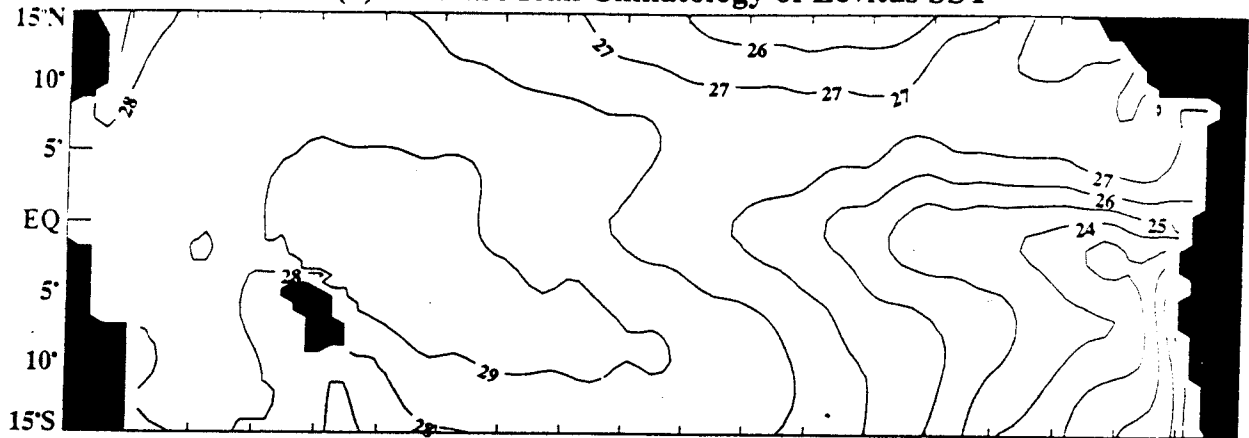
(b) KPP Simulation



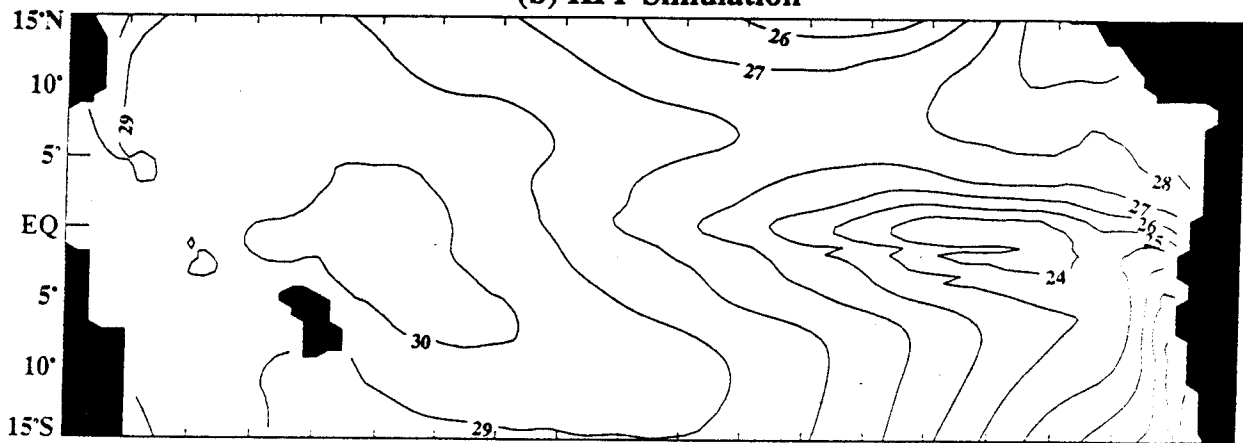
(c) PP Simulation



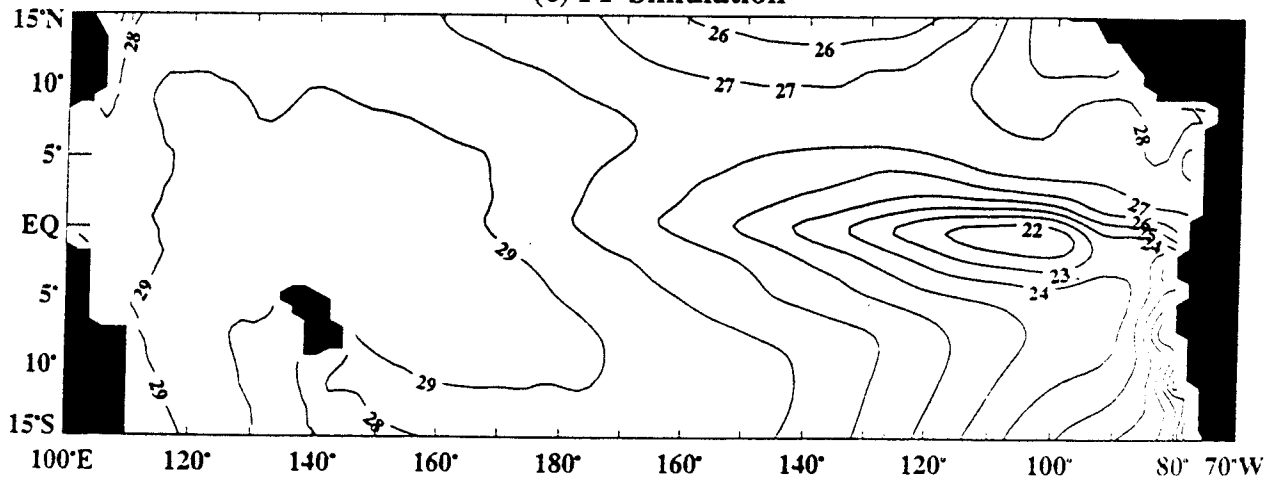
(a) Annual Mean Climatology of Levitus SST



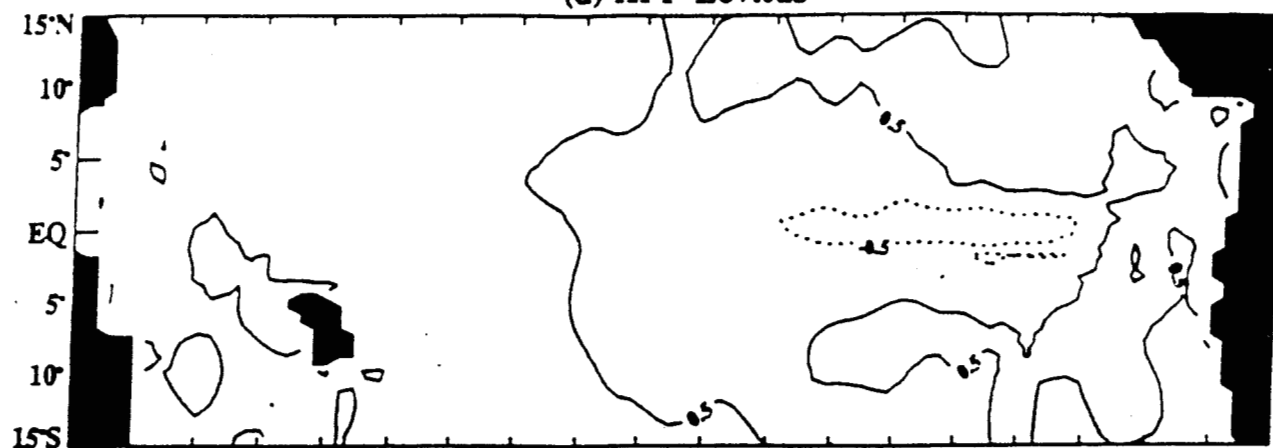
(b) KPP Simulation



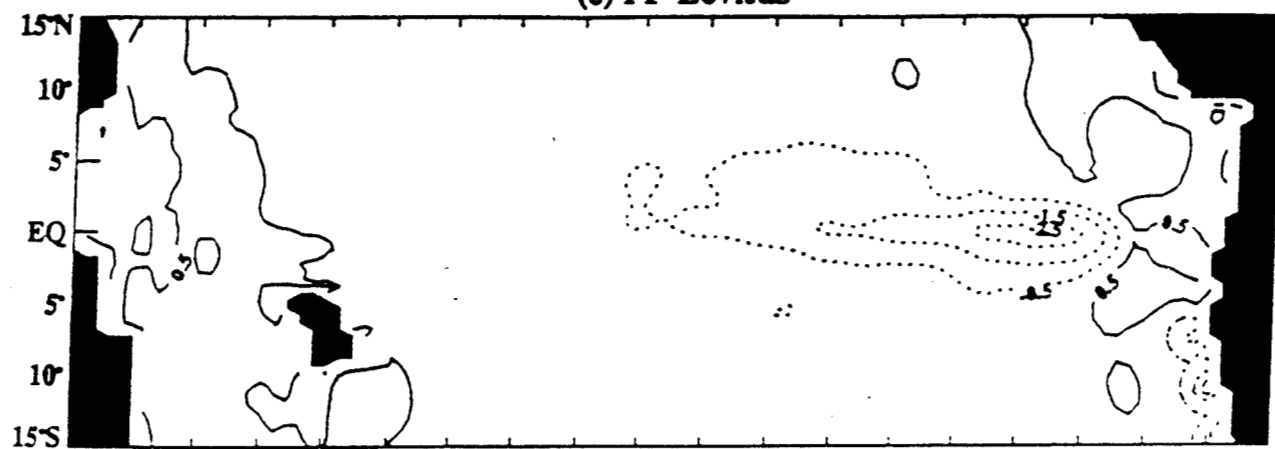
(c) PP Simulation



(d) KPP-Levitus



(e) PP-Levitus



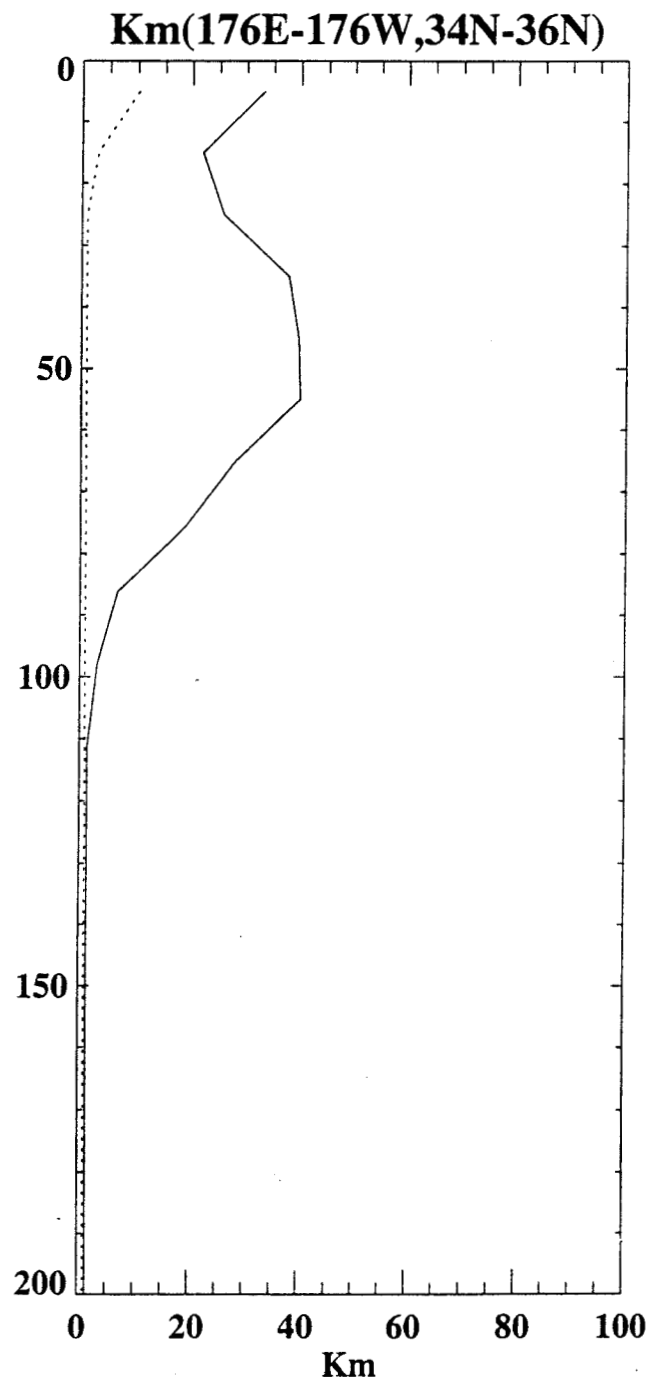


Fig. 5

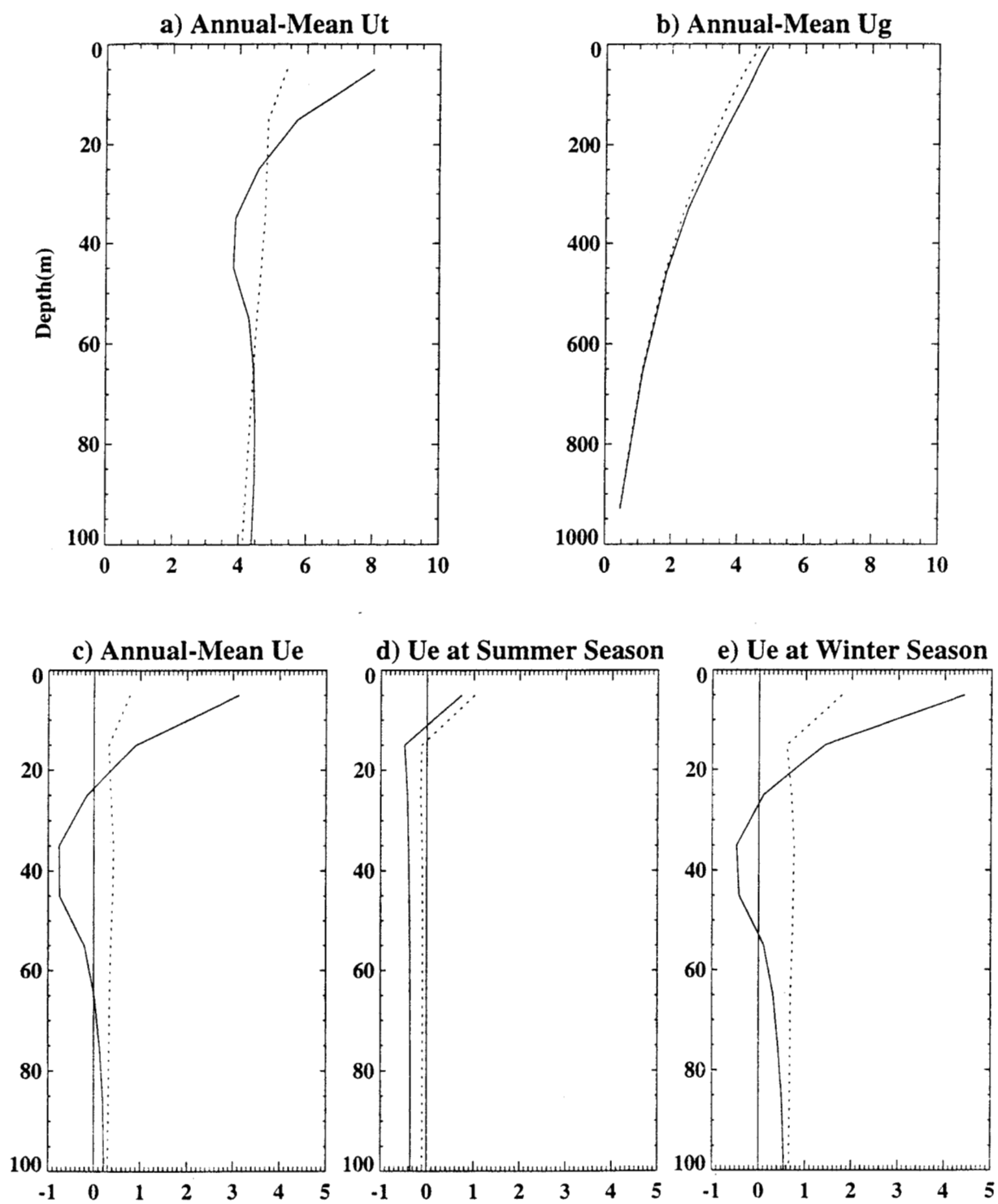
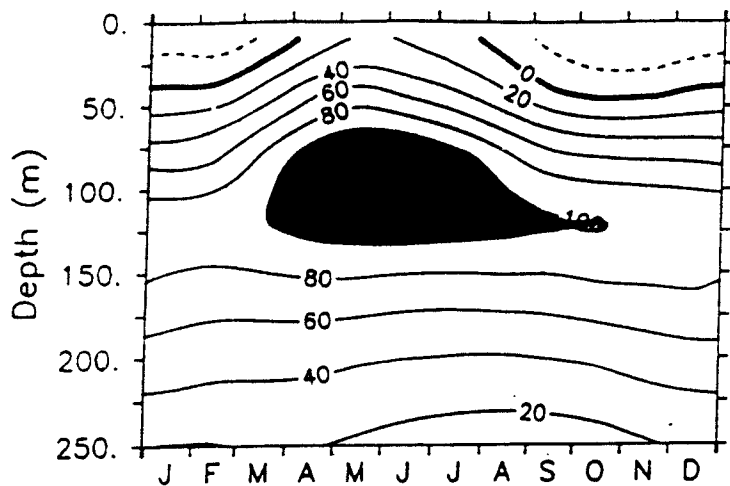
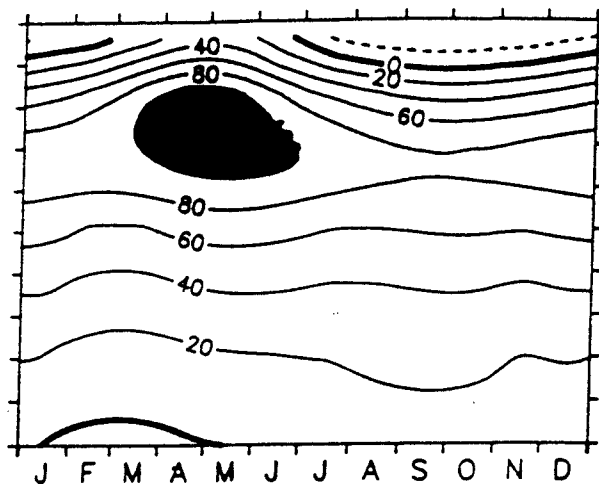


Fig. 6

0°, 140°W Climatologies

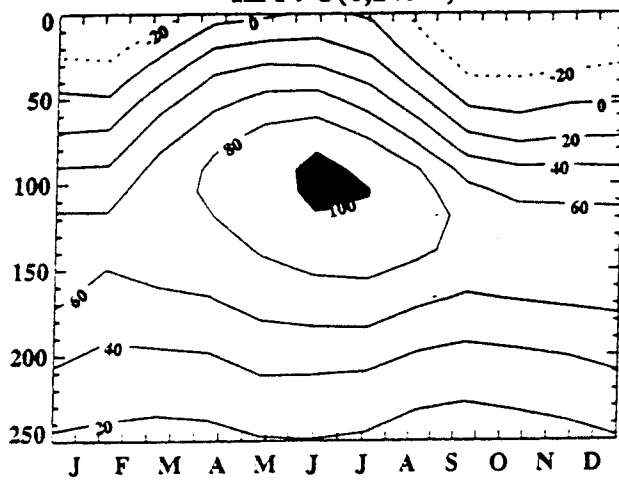


0°, 110°W Climatologies

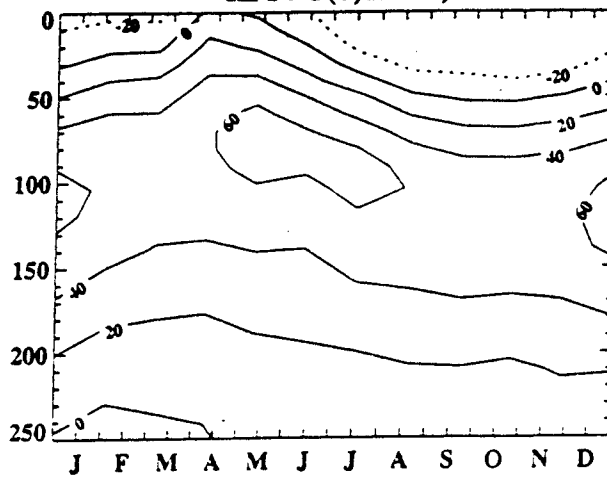


U

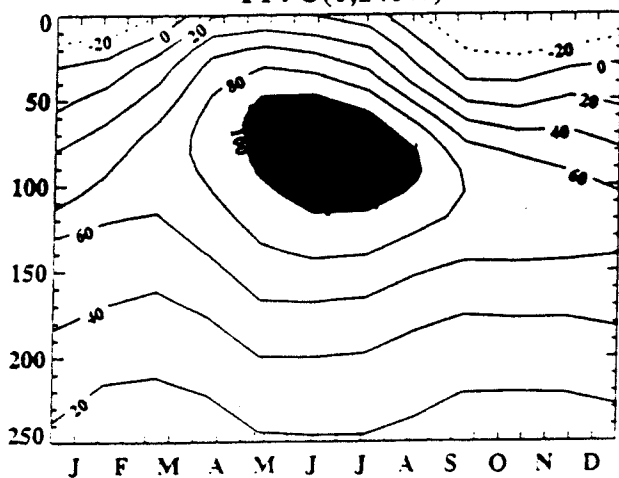
KPP: U(0,140W)



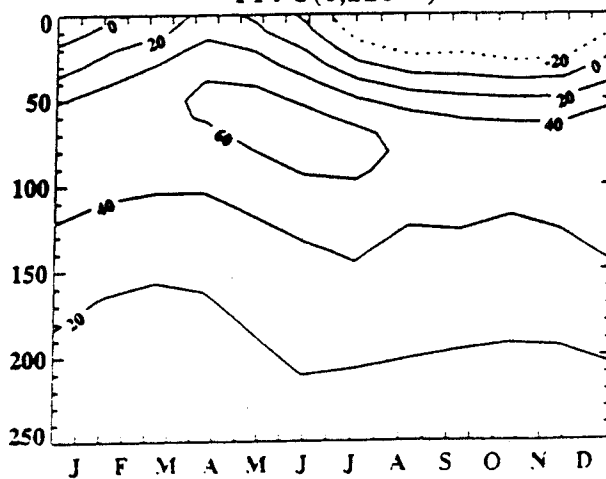
KPP: U(0,110W)

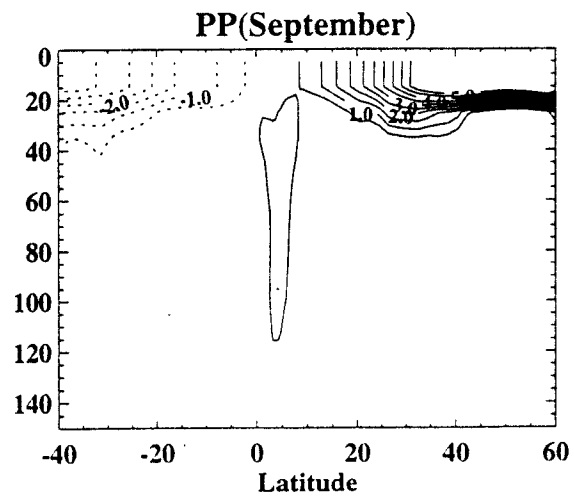
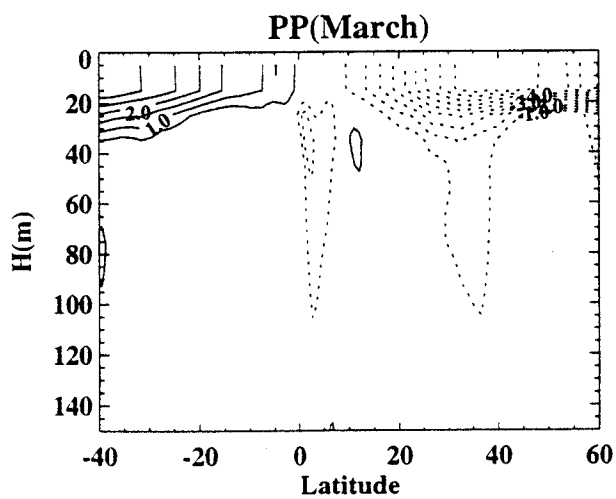
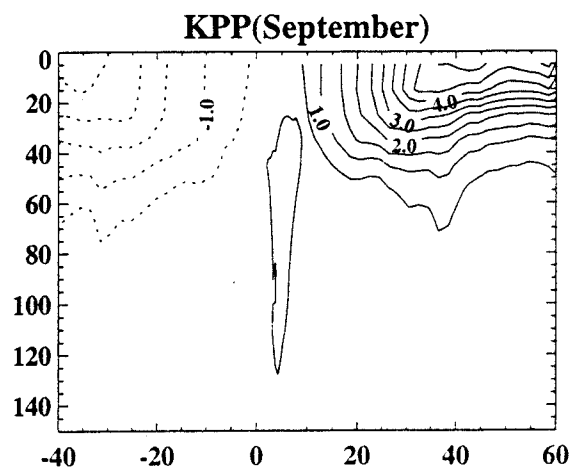
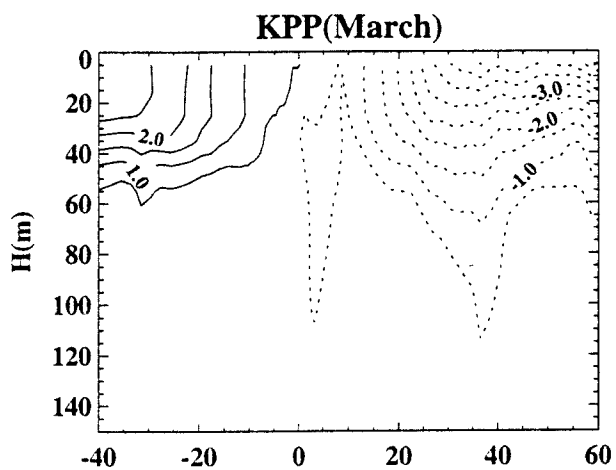
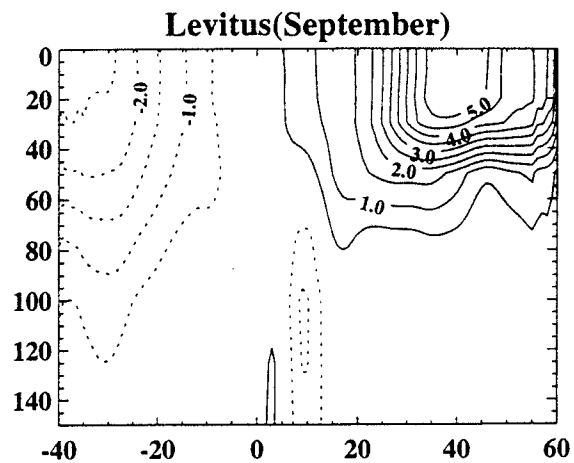
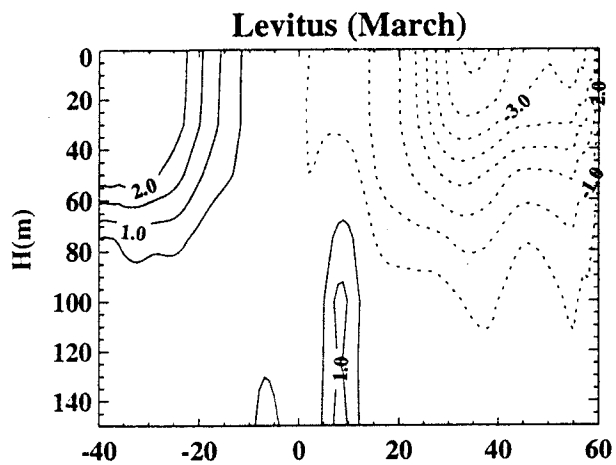


PP: U(0,140W)

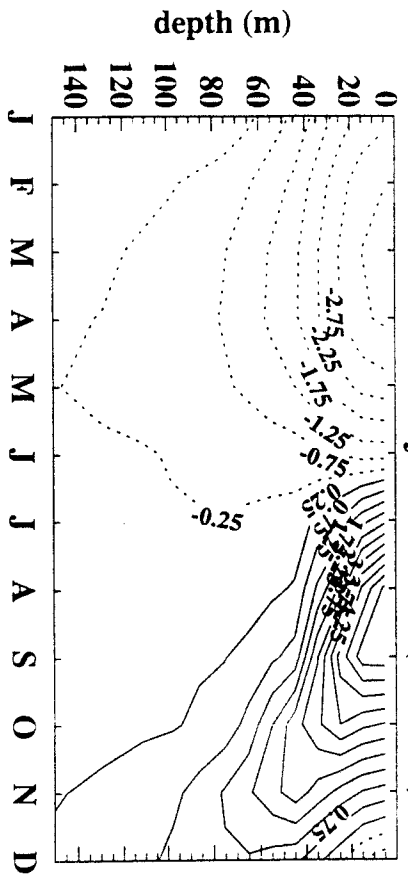


PP: U(0,110W)

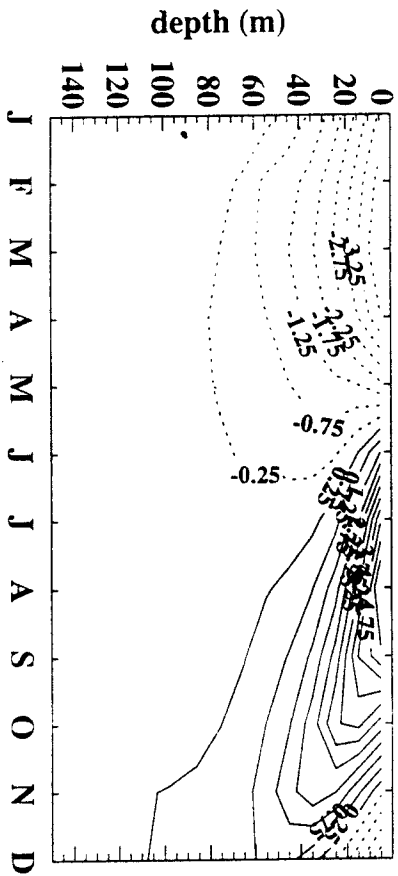




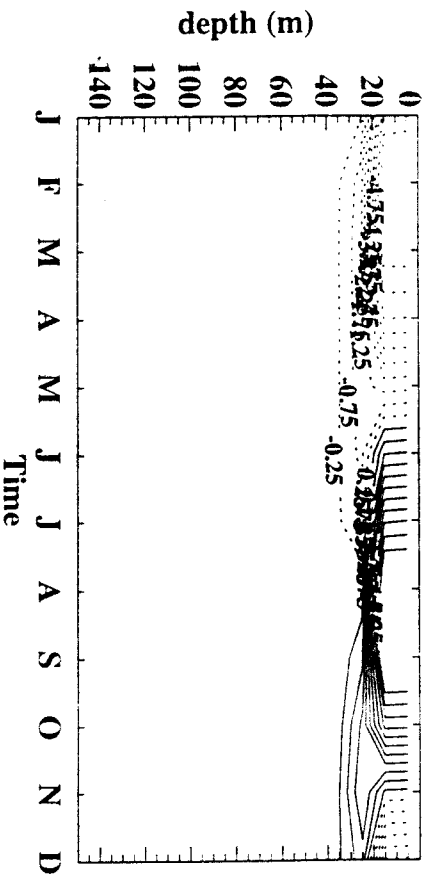
a. T Seasonal Cycle at 40N (Levitus)



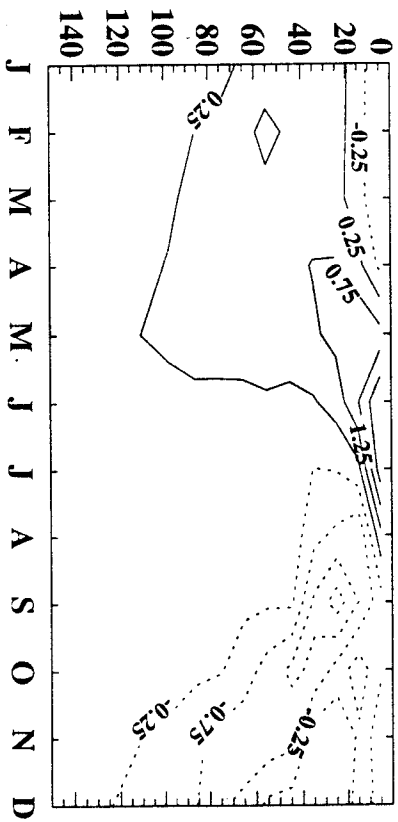
b. KPP



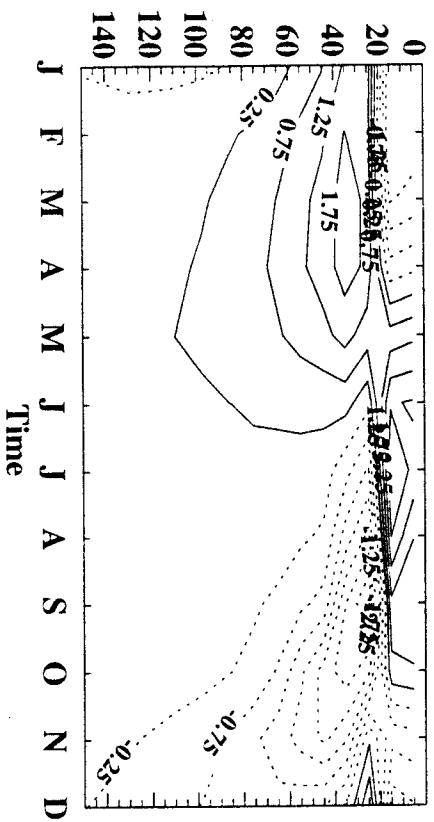
c. PP



d. KPP-Levitus



e. PP-Levitus



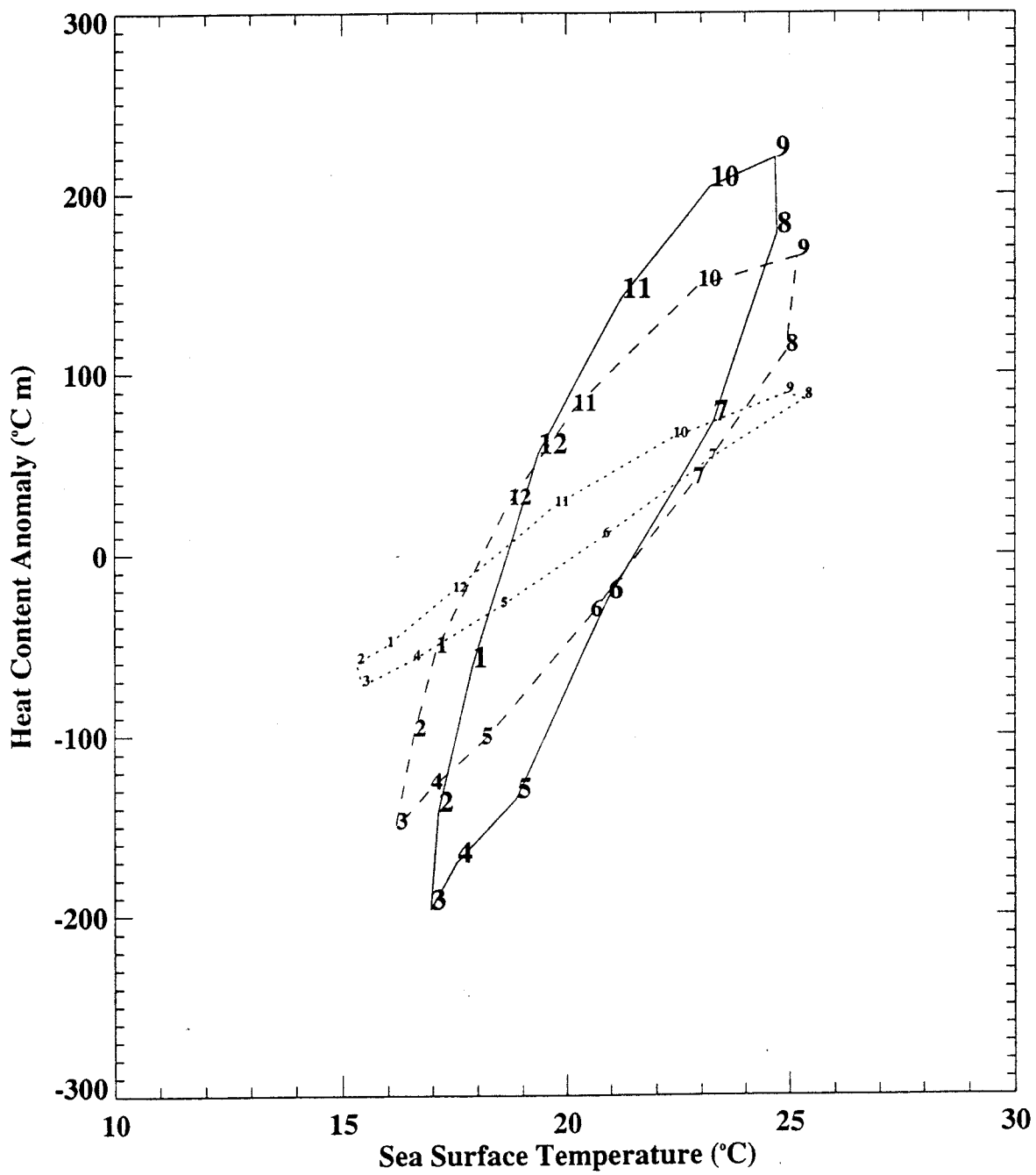
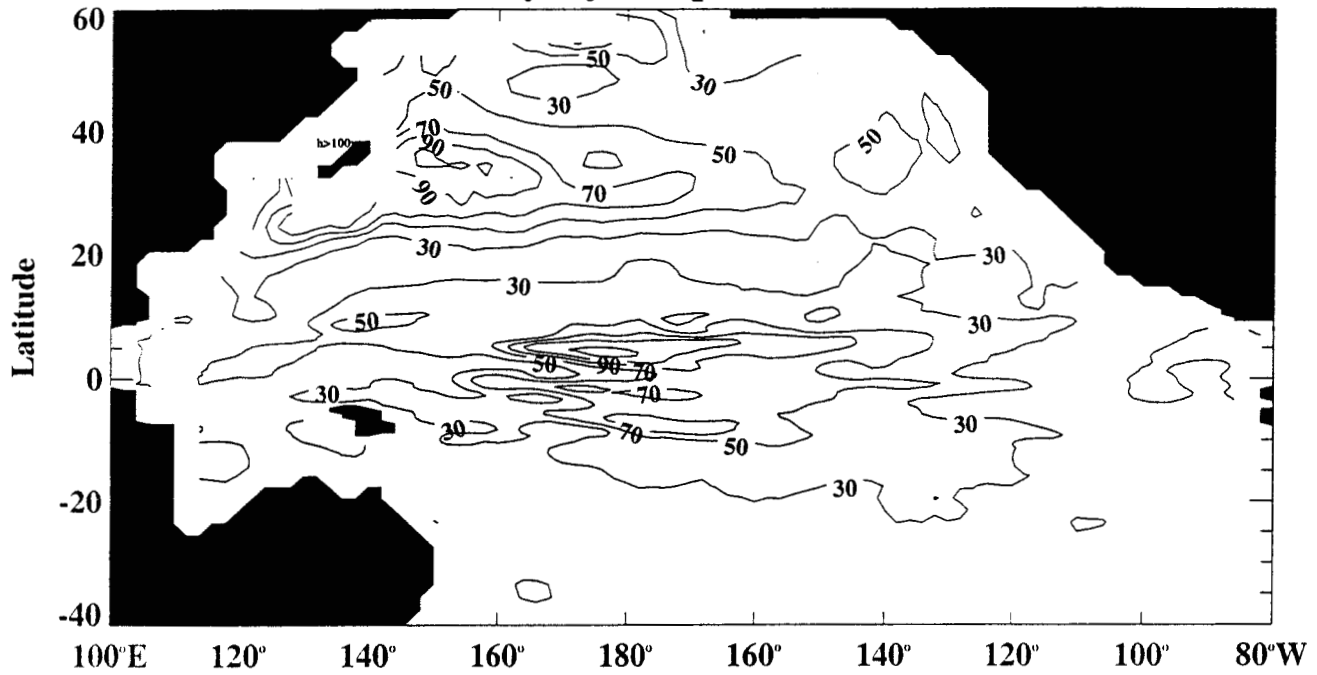
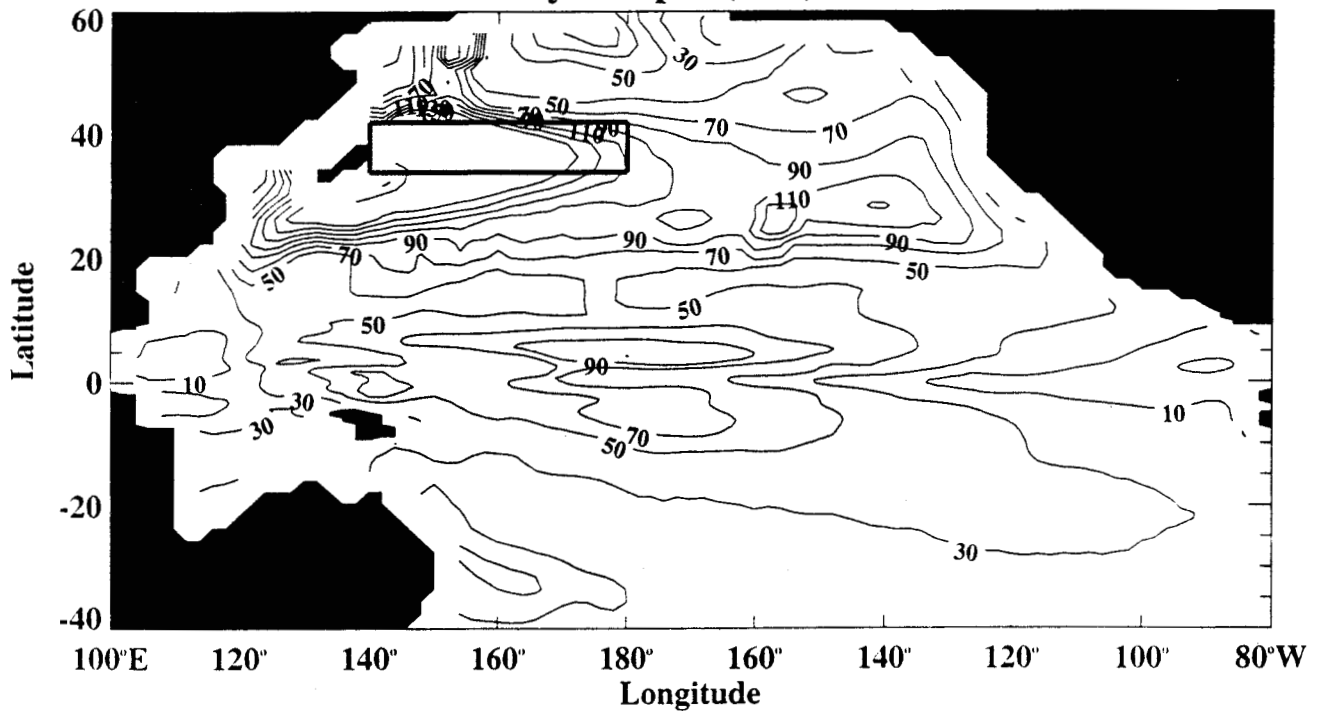


Fig. 10

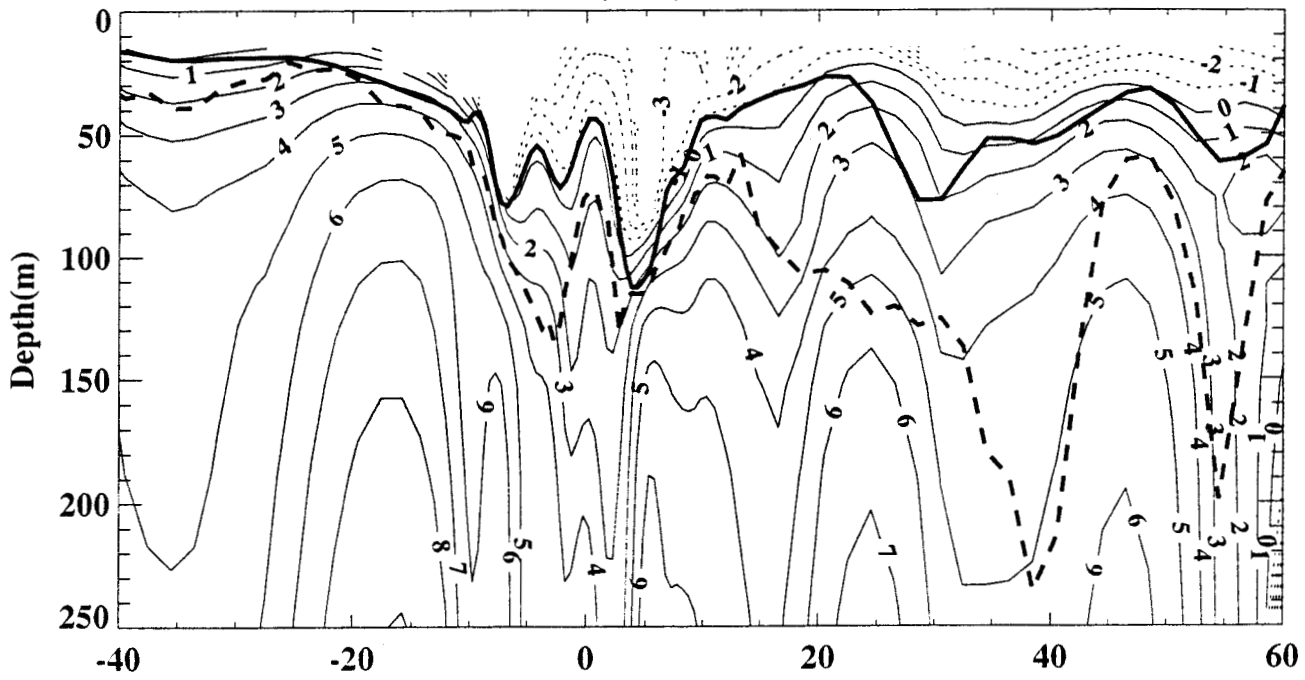
Boundary layer depth (hbl) in March



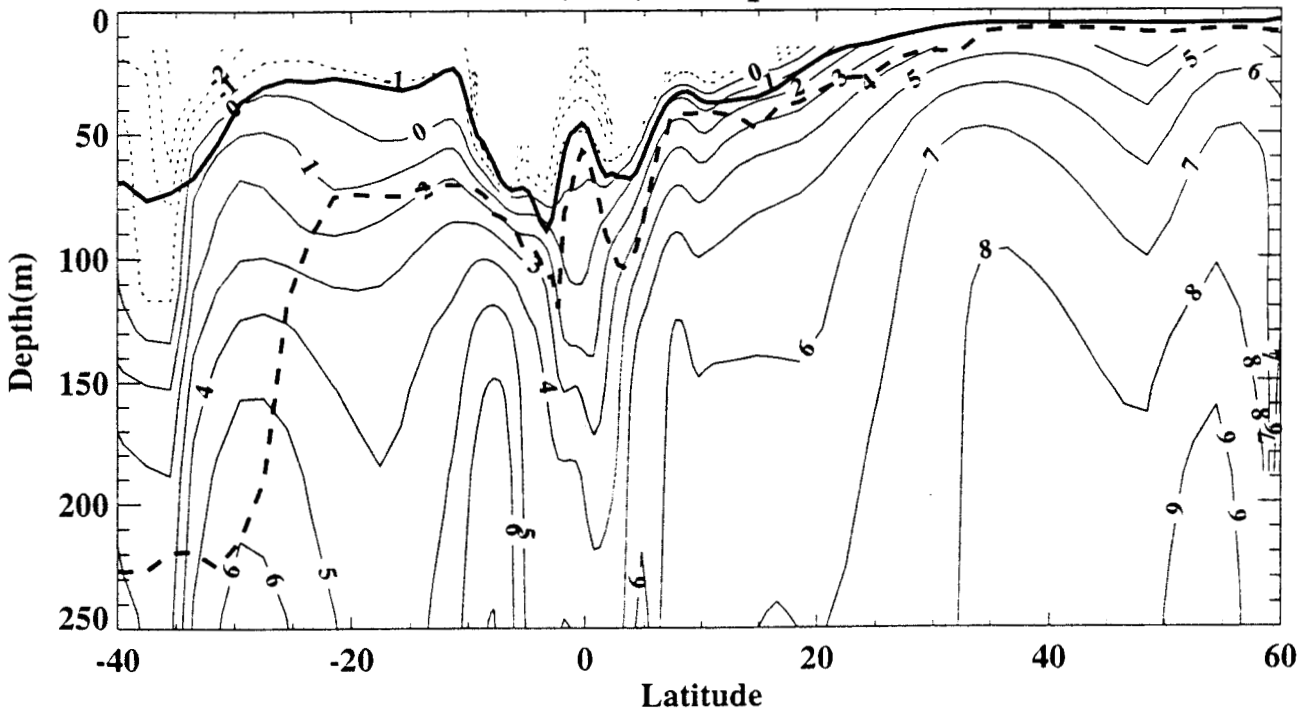
Mixed layer depth (mld) in March

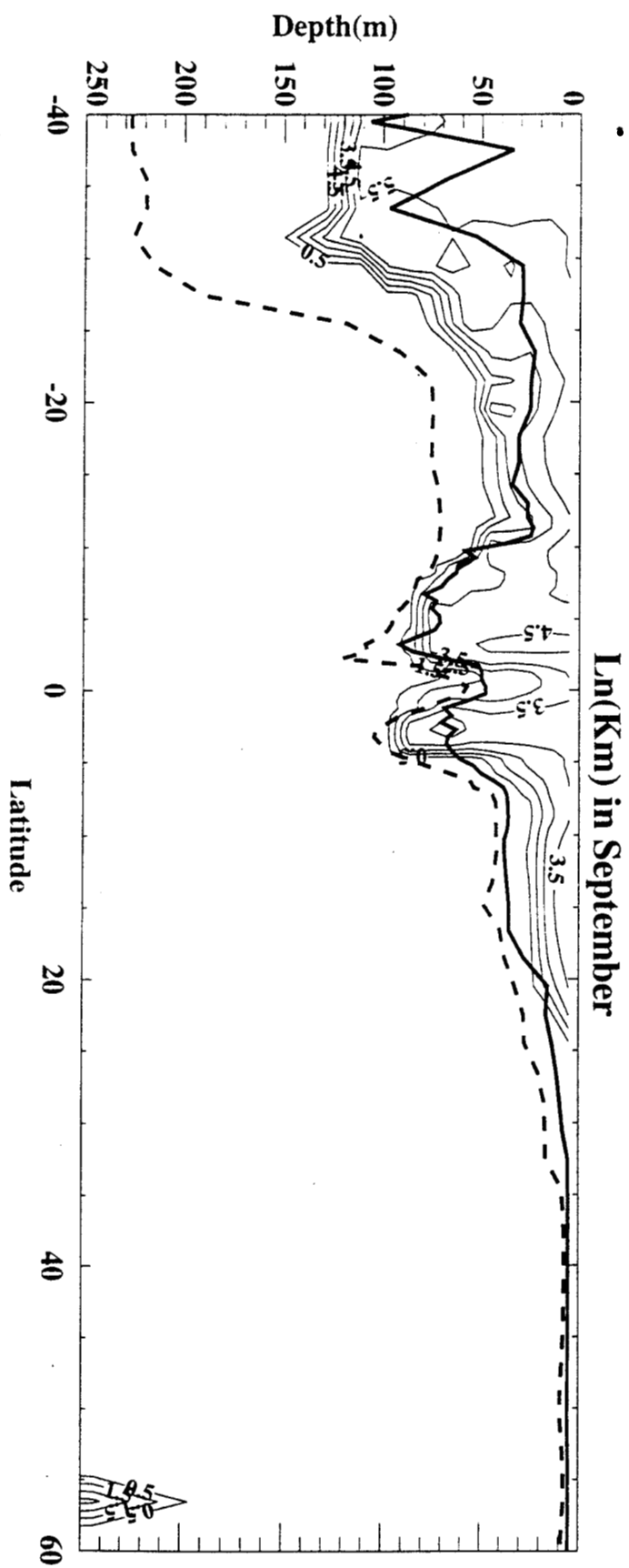
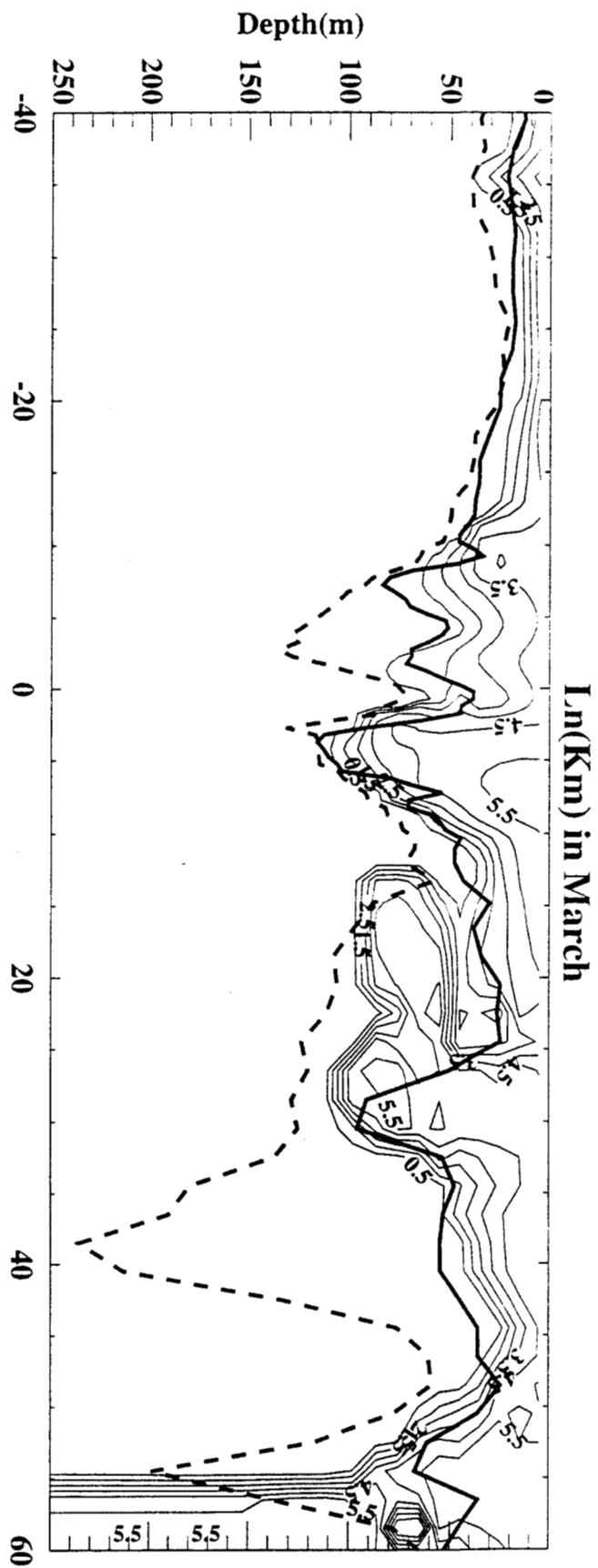


Ln(Rib) in March

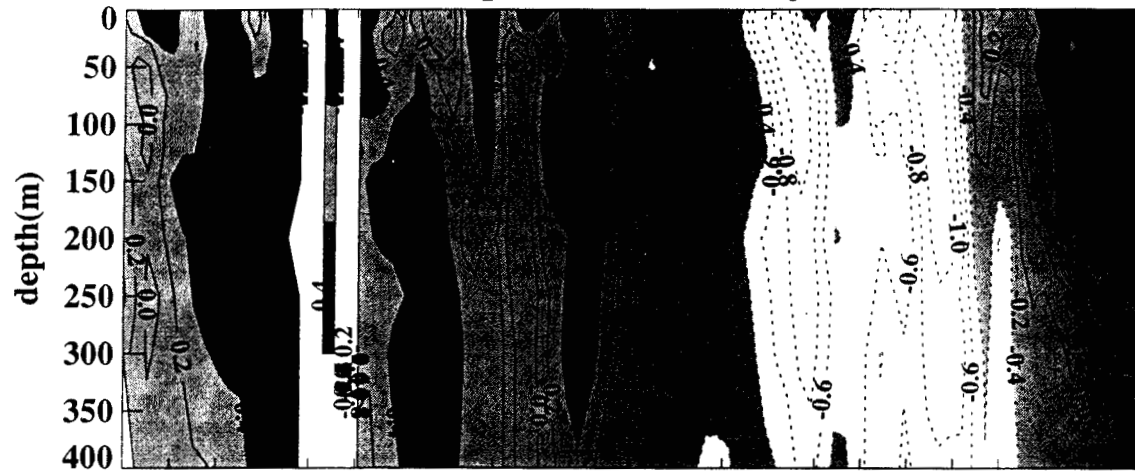


Ln(Rib) in September

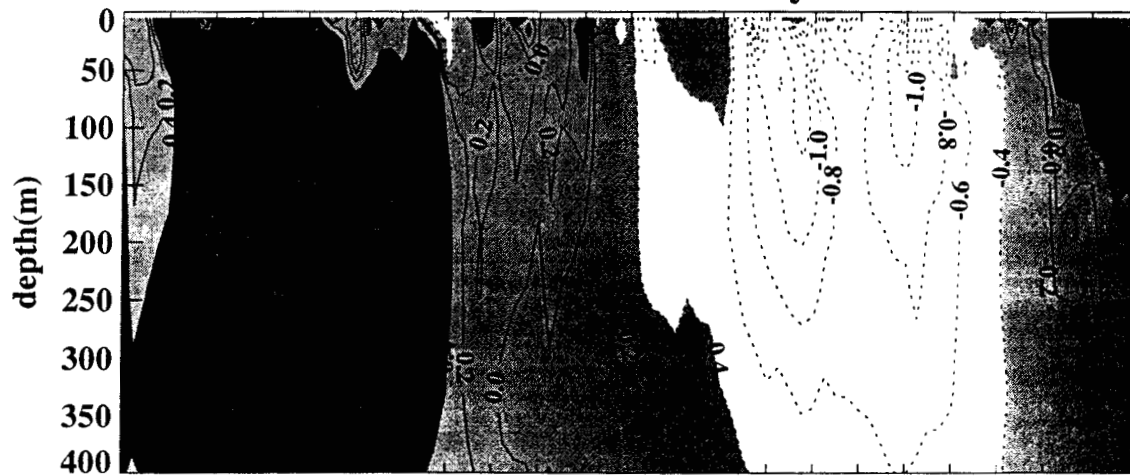




Observed Temperature Anomaly (TA) at KCE



Simulated TA at KCE by KPP



Simulated TA at KCE by PP

